

## Flow-pattern identification for two staggered circular cylinders in cross-flow

By D. SUMNER,<sup>†</sup> S. J. PRICE AND M. P. PAÏDOUSSIS

Department of Mechanical Engineering, McGill University, 817 Sherbrooke Street West, Montréal, Québec, Canada H3A 2K6

(Received 23 December 1998 and in revised form 12 January 2000)

The flow around two circular cylinders of equal diameter, arranged in a staggered configuration, was investigated using flow visualization and particle image velocimetry for centre-to-centre pitch ratio  $P/D = 1.0$  to  $5.0$  and angle of incidence  $\alpha = 0^\circ$  to  $90^\circ$ . Experiments were conducted within the low subcritical Reynolds number regime, from  $Re = 850$  to  $1900$ . Nine flow patterns were identified, and processes of shear layer reattachment, induced separation, vortex pairing and synchronization, and vortex impingement, were observed. New insight was gained into previously published Strouhal number data, by considering the flow patterns involved. The study revealed that vortex shedding frequencies are more properly associated with individual shear layers than with individual cylinders; more specifically, the two shear layers from the downstream cylinder often shed vortices at different frequencies.

### 1. Introduction

By virtue of its common occurrence in many forms and in different applications, both in nature and technology, fluid flow around a circular cylinder has been well studied, and is one of the classical problems of fluid dynamics. Cylinder-like structures can be found, both alone and in groups, for example in the designs for heat exchangers, cooling systems for nuclear power plants, offshore structures, buildings, chimneys, power lines, struts, grids, screens, and cables, in both air and water flow. In many of these engineering applications, the periodic shedding of Kármán vortices is responsible for problems with flow-induced vibration and noise. A complete understanding of the fluid dynamics for the flow around a circular cylinder encompasses such fundamental subjects as the boundary layer, the free shear layer, the wake and the dynamics of vortices.

Less well studied and understood are the modifications to the fluid dynamics of a single circular cylinder which may occur when two or more circular cylinders are placed in close proximity to one another. The flow field of a multiple cylinder configuration may involve complex interactions between the shear layers, vortices and Kármán vortex streets. Many of these effects have been compiled in review articles by Zdravkovich (1977, 1987, 1993), Nishimura (1986) and Ohya, Okajima & Hayashi (1989). The staggered configuration is the most general form of two cylinders in close proximity, arranged at arbitrary centre-to-centre spacing and arbitrary angle of incidence to the oncoming flow, and it is perhaps the configuration most commonly found in engineering applications. Its fluid dynamics, however, apart from measurements of

<sup>†</sup> Present address: Department of Mechanical Engineering, University of Saskatchewan, 57 Campus Drive, Saskatoon, Saskatchewan, S7N 5A9, Canada.

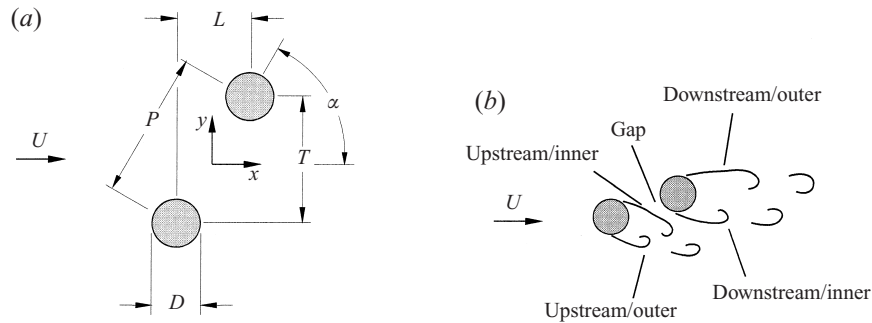


FIGURE 1. Staggered configuration of two circular cylinders of equal diameter in steady cross-flow: (a) notation; (b) shear layer and vortex designations.

the fluid forces acting upon the cylinders and the frequencies of vortex shedding, has been the subject of rather limited study.

The present study, of a simple configuration of two circular cylinders of equal diameter arranged in a general, staggered configuration, in steady cross-flow, has been motivated by both fundamental and practical considerations. The primary objective was to acquire, through experiments, an improved physical understanding of the fluid dynamics of the staggered configuration. Flow patterns were identified using two complementary investigative techniques: dye injection flow visualization with a video camera, and instantaneous velocity and vorticity data acquired with particle image velocimetry (PIV). The fluid behaviour was then gauged through changes in the flow patterns, as the spacing between the cylinders and the orientation of the cylinders with respect to the oncoming flow were varied.

## 2. Background

The geometry of the staggered pair of cylinders, each of equal diameter  $D$ , immersed in steady cross-flow of velocity  $U$ , is set by the centre-to-centre pitch  $P$  between the cylinders and the angle of incidence  $\alpha$  as shown in figure 1. Alternatively, it may be defined by the longitudinal and transverse spacings  $L$  and  $T$ , also shown in figure 1.

### 2.1. Review of previous work

Previous studies of the staggered configuration, by Suzuki *et al.* (1971), Ishigai *et al.* (1972), Ishigai, Nishikawa & Yagi (1973), Price (1976), Zdravkovich & Pridden (1977), Kiya *et al.* (1980), Price & Paidoussis (1984), Moriya & Sakamoto (1985), Sun *et al.* (1992), and Gu & Sun (1999), have revealed considerable complexity in the fluid dynamics, as  $P/D$  and  $\alpha$  are varied. These studies are summarized in table 1. The complexity lies in the interaction of four separated free-shear layers, two Kármán vortex formation and shedding processes, and interactions between the two Kármán vortex streets (figure 1b). Unfortunately, few extensive flow visualization studies have been undertaken for two staggered cylinders from which the complexity of the flow in the near wake can be understood. Some flow visualization photographs may be found in the work of Suzuki *et al.* (1971), Ishigai *et al.* (1972, 1973), Price (1976), Moriya & Sakamoto (1985), and Gu & Sun (1999). However, no systematic study using flow visualization is undertaken in these studies. Furthermore, the effects of Reynolds number have yet to be examined in any study of the staggered geometry to date, and such an investigation would likely reveal further variation to the flow

Researchers	$Re$	Geometry	Facility	Technique	AR	Blockage	$TI_u$	Measurements
Gu & Sun (1999)	5600	$P/D = 1.5\text{--}2.0$ $\alpha = 0^\circ\text{--}45^\circ$	Wind tunnel	FV	not given	not given	not given	—
Gu & Sun (1999)	$2.2 \times 10^5\text{--}$ $3.3 \times 10^5$	$P/D = 1.1\text{--}3.5$ $\alpha = 0^\circ\text{--}90^\circ$	Wind tunnel	Pressure	6.4	8%	0.2%	a, b, d, e, h
Ishigai <i>et al.</i> (1972, 1973)	1500–15 000	$L/D = 0.68\text{--}4.0$ $T/D = 0.5\text{--}3.0$	Wind tunnel	FV, CTA, pressure	11	9%	not given	a, b
Kiya <i>et al.</i> (1980)	20 000– 37 000	$P/D = 0.0\text{--}5.5$ $\alpha = 0^\circ\text{--}90^\circ$	Wind tunnel	CTA	11	19%	0.8%	a
Moriya & Sakamoto (1985)	65 300	$L/D = 2.0\text{--}6.0$ $T/D = 0.0\text{--}1.5$	Wind tunnel	Force balance, FV, pressure	10	20%	0.4%	a, b, c, d, e, f, g
Price (1976)	17 000– 80 000	$L/D = 6.0\text{--}18.0$ $T/D = 0.0\text{--}2.42$	Wind tunnel	Force balance, FV, pressure	37, 42	5–12%	1.0–11.0%	b, d, e
Price & Paidoussis (1984)	17 000– 86 000	$L/D = 1.5\text{--}5.0$ $T/D = 0.75\text{--}2.0$	Wind tunnel	Force balance	24	6%	0.5%	d, e
Sun <i>et al.</i> (1992)	$3.25 \times 10^5\text{--}$ $6.5 \times 10^5$	$P/D = 2.2$ $\alpha = 12.5^\circ$	Wind tunnel	Pressure	15	10%	0.12–10.0%	b, c
Suzuki <i>et al.</i> (1971)	1300	$P/D = 2.0$ $\alpha = 0^\circ\text{--}15^\circ$	Water tunnel	FV	not given	not given	not given	—
Suzuki <i>et al.</i> (1971)	$1 \times 10^5\text{--}$ $6.3 \times 10^5$	$P/D = 1.1\text{--}3.9$ $\alpha = 0^\circ\text{--}15^\circ$	Wind tunnel	Pressure	6–18	12–24%	not given	b, d
Zdravkovich & Pridden (1977)	60 000	$L/D = 0.0\text{--}5.0$ $T/D = 0.0\text{--}3.0$	Wind tunnel	Force balance, pressure	33	5%	0.1%	b, d, e
Current study	850–1350	$P/D = 1.0\text{--}5.0$ $\alpha = 0^\circ\text{--}90^\circ$	Water tunnel	FV	16	13%	0.5%	a
Current study	1900	$P/D = 1.0\text{--}4.0$ $\alpha = 0^\circ\text{--}90^\circ$	Towing tank	PIV	27	7%	—	h, i

TABLE 1. Experimental investigations of two staggered circular cylinders of equal diameter in steady upstream cross-flow. Measured quantities: (a) Strouhal number, (b) mean surface pressure distribution, (c) r.m.s. surface pressure distribution, (d) mean drag coefficient, (e) mean lift coefficient, (f) r.m.s. drag coefficient, (g) r.m.s. lift coefficient, (h) velocity field, (i) vorticity field. Abbreviations: FV = flow visualization; CTA = constant-temperature anemometry; PIV = particle image velocimetry. Blockage ratio based on total blockage for two cylinders.

patterns. This configuration has been studied mostly at high subcritical Reynolds numbers (defined for a single circular cylinder), since these are more commonly found in industrial applications.

Previous studies have typically acquired information on the vortex shedding frequencies and the lift and drag forces. The vortex shedding frequency,  $f_s$ , is usually expressed in non-dimensional form as the Strouhal number,  $St (= f_s D/U)$ . Of particular concern have been specific staggered geometries that give rise to extreme values of the lift force or drag force (Price 1976; Zdravkovich & Pridden 1977; Moriya & Sakamoto 1985). A number of different explanations for the origin of the lift force have been provided in the literature, which were recently summarized by Ting *et al.* (1998).

## 2.2. Approaches to understanding the fluid dynamics

In previous studies, a number of approaches have been used in an attempt to classify the fluid behaviour around multiple circular cylinders in steady cross-flow. The simplest approach is by Zdravkovich (1987), who classified the fluid behaviour into two basic types of interference, based on the location of the downstream cylinder with respect to the upstream one: (i) wake interference, when one of the cylinders is partially or completely submerged in the wake of the other, and (ii) proximity interference, when the two cylinders are located close to one another, but neither is submerged in the wake of the other. A recent study by Gu & Sun (1999) has extended this classification to three different types, namely wake interference, shear layer interference, and neighbourhood interference. Both these classifications, however, fail to recognize the complex behaviour displayed in experiments and the wide range of flow patterns observed. As the present study has shown, even the 'no-interference' region of Zdravkovich (1987) is a misnomer, since interference in the form of anti-phase synchronization of the vortex shedding processes (Williamson 1985; Sumner *et al.* 1999) is found there.

A second approach has been through the interpretation of experimental data; specifically, vortex shedding frequencies, static pressure measurements on the cylinder surfaces, and lift and drag forces. As examples: (i) vortex shedding frequency data have been used to infer the existence of two Kármán vortex shedding processes for staggered cylinder configurations, by Kiya *et al.* (1980); (ii) static pressure coefficient data have been offered as evidence of a stable pair of eddies within the gap between two tandem cylinders ( $\alpha = 0^\circ$ ), and continuous reattachment of the two shear layers, by Igarashi (1981, 1984); and (iii) peak lift force measurements for two staggered cylinders, and rapid changes in the lift force for small adjustments to the geometry, have been attributed to the strong influence of the high-speed flow deflected through the gap between cylinders, as described by Zdravkovich & Pridden (1977). Such an approach is useful from an engineering design point of view, and has led to many recommendations for avoiding the occurrence of flow-induced vibration, for instance. However, determining the fluid behaviour from measured quantities is prone to misinterpretation, particularly when done without the benefit of accompanying flow visualization.

A third approach to understanding the fluid dynamics of multiple cylinders in cross-flow, and arguably the most useful, is to identify from flow visualization (and other means) the various flow patterns which arise for different choices of the geometry. The understanding of the fluid dynamics of tandem cylinders in cross-flow has greatly benefited from this approach, as demonstrated, for example, by Igarashi (1981, 1984). His studies identified up to eight different flow patterns from a combination of flow

visualization and measured data for various combinations of  $L/D$  and the Reynolds number,  $Re$ . Equally spaced clusters of three and four cylinders have also been investigated with remarkable effectiveness through the flow pattern approach, by Lam & Cheung (1988) and Lam & Lo (1992).

The flow pattern approach has not been extensively pursued, to date, for the staggered configuration. Only the recent work of Gu & Sun (1999), mentioned earlier, has attempted to identify some flow patterns, although their flow visualization experiments were conducted solely from  $P/D = 1.5$  to 2.0. Consequently, one of the primary objectives of the present study has been to consider a complete range of two-cylinder configurations in cross-flow from a common, flow-pattern approach.

### 3. Experimental approach

A two-fold experimental approach was followed which combined conventional dye-injection flow visualization and particle image velocimetry (PIV). This approach is similar to that followed in a recent study of side-by-side cylinders ( $\alpha = 90^\circ$ ) in steady upstream cross-flow (Sumner *et al.* 1999). The flow visualization experiments were conducted first, in a closed-test-section water tunnel, to gain a preliminary understanding of the fluid behaviour.

The flow visualization images were also used to estimate the vortex shedding frequencies in the flow fields, a process which, when carefully done, yielded an uncertainty of 5% in the Strouhal number. In this method, the observer counts, with the aid of a stopwatch, the number of vortices shed from a given shear layer that are convected past a given reference point in the image.

The PIV experiments were conducted next, in a towing tank. This facility was purposely built for PIV experiments in steady and unsteady flows (Sumner 1999). The interpretation of the instantaneous, in-plane velocity and vorticity fields provided by the PIV technique was greatly aided by the flow visualization experiments conducted beforehand. Direct correspondence between the two techniques on a qualitative basis, while possible, is not always easy, however. The dye streaklines illustrate the vorticity field, but tend to show the 'integrated' effects of the fluid motion. In contrast, the PIV vorticity data give an instantaneous representation of the fluid motion, meaning that the flow structures more easily identified in the video images are less easily identified from the vorticity data. Some of the difficulties in correspondence between the flow visualization images and the PIV data may also be attributed to the low spatial resolution of the current PIV set-up (see § 3.2).

#### 3.1. Flow visualization experiments

The dye-injection flow visualization experiments were conducted in a Kempf & Remmers closed-loop water tunnel, with a 254 mm  $\times$  254 mm cross-section working section, and a longitudinal free-stream turbulence intensity of 0.5%. The cylinder models, with  $D = 16$  mm, were constructed of Plexiglas. The cylinder aspect ratio was 16 and the solid blockage ratio (per cylinder) was 6.3%, meaning the maximum blockage encountered in any of the experiments was 12.6%. No end-plates were fitted to the cylinders in the water tunnel experiments. Each cylinder had two dye injection ports of 0.8 mm diameter located at mid-span and near the points of boundary layer separation. For flow visualization, fluorescein and rhodamine dyes were injected into the near-wake regions of the cylinders. The dye streaklines were illuminated using a narrow sheet of light from a xenon arc lamp. The fluid motion was captured with a JVC KY-25U Super-VHS video camera. Although a still camera could have

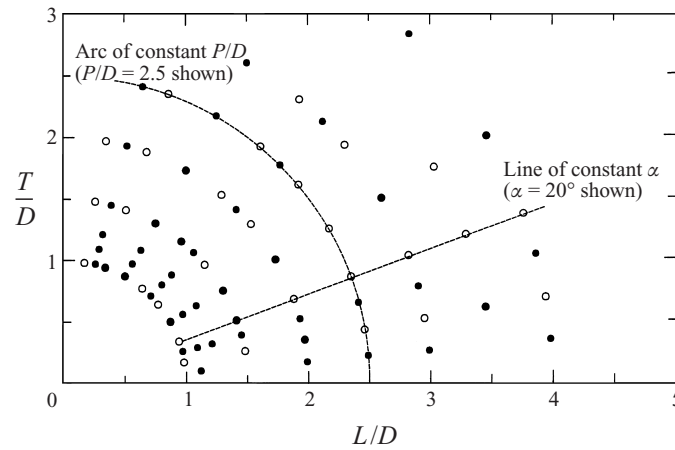


FIGURE 2. Staggered configurations tested in the present study,  $L/D$ – $T/D$  notation:  
 ○, flow visualization experiments; ●, PIV experiments.

provided higher-quality images, of greater resolution, a single image (or a series of single images) is not sufficient to fully characterize the dynamic behaviour of the flow, for a given cylinder group. By studying the video, a more detailed description of the flow physics could be developed. The video also made it easier to isolate and capture specific structures in the flow field. By opting to use video, however, the problem of how to effectively reproduce videotaped results, in print and in a limited amount of space, remains. Here, individual video frames which were judged to best illustrate key aspects of the flow were selected for reproduction in the paper; they were printed with a video printer, scanned with a high-resolution scanner, and enhanced with Adobe PhotoShop software. Much of the authors' interpretation of the flow, found later in the paper, is based on the video images.

These experiments examined staggered configurations corresponding to various combinations of nine pitch ratios, from  $P/D = 1.0$  to  $5.0$ , and eight angles of incidence, from  $\alpha = 10^\circ$  to  $80^\circ$  in steps of  $10^\circ$  (see figure 2). The flow was visualized only for a limited range of Reynolds number,  $Re = 850$  to  $1350$ . This range was selected based on the quality of the flow visualization, since at higher velocities the dyes tended to diffuse more rapidly.

### 3.2. PIV experiments

The PIV experiments were undertaken in a towing tank, of  $0.76 \text{ m} \times 0.76 \text{ m}$  cross-section and  $3.05 \text{ m}$  length. The tank walls were constructed of glass. Each cylinder was constructed of stainless steel, with  $D = 25.4 \text{ mm}$  and an aspect ratio of 27. Each cylinder had a solid blockage ratio of 3.5%, meaning the maximum blockage encountered in the experiments was 7%. A single end-plate made from Plexiglas was fitted to the multiple cylinder configuration at the free end near the bottom of the tank, based on the optimized design of Szepessy (1993) for a single cylinder. End effects near the free surface and the end-plate were found to be confined to spanwise distances of approximately 7 diameters. This meant that the central portion of the span of 13 diameters was subject to nominally two-dimensional flow conditions (Sumner 1999). The experiments were conducted at  $Re = 1900$ , for staggered arrangements corresponding to various combinations of nine pitch ratios, from  $P/D = 1.0$  to  $4.0$ , and nine angles of incidence, from  $\alpha = 5^\circ$  to  $75^\circ$  (see figure 2).

For the application of PIV, the water was seeded with irregularly shaped, nearly neutrally buoyant particles, of 100 to 300  $\mu\text{m}$  in size. A section of the flow was illuminated with a pulsed light sheet, generated by a 5 W argon-ion laser and a mechanical shutter. Successive pairs of single-exposed digital particle images (each of  $512 \times 480$  pixels) were acquired with a Dantec Double Image 700 CCD camera and frame grabber. The horizontal image magnification was of the order of  $M_x = 0.3 \text{ mm/pixel}$ , and each image covered an area of approximately  $150 \times 150 \text{ mm}$  ( $6 \times 6$  cylinder diameters) within the flow field. The image exposure time was typically 6 ms, and the time between single-exposed images constituting a pair was typically 4 ms. In the 10 ms time difference between the images comprising a pair, a particle moving at the free-stream velocity of  $75 \text{ mm s}^{-1}$  would cover 2.5 pixels (0.75 mm or 0.03 diameters). Given that the cylinders were opaque, it was not possible for the entire flow field to be illuminated with the light sheet. The light source was placed in such way as to illuminate the combined wake region of the cylinders, with the 'shadow' created by the cylinders oriented obliquely toward the cross-stream and towing directions. To aid the reader, the 'shadow' region is identified in the vorticity plots in figures 5 and 6.

The camera was mounted in a fixed position beneath the towing tank. Images were acquired, with the aid of a mirror, through the glass bottom of the towing tank and through the Plexiglas end-plate. The light sheet was located at the centre-span of the cylinder midway between the free surface of the water and the end-plate. Images were acquired near the end of a towing run of about 2.5 m, in order to minimize the influence of transient effects related to the start-up of the towing. At  $Re = 1900$ , this distance corresponds to a non-dimensional elapsed time from the start of towing of  $t^* = tU/D = 98$  (for elapsed time  $t$  from the start of motion).

Dantec FlowGrabber digital PIV software employing the cross-correlation algorithm of Willert & Gharib (1991) was used to compute the raw displacement vector field from the particle image data. An interrogation window of  $32 \times 32$  pixels (approximately  $10 \times 10 \text{ mm}$ , or  $0.3 \times 0.3$  cylinder diameters), with 75% overlap, was used. The size of the interrogation window effectively limited the minimum size of the vortex structures that can be identified in these experiments to approximately 0.3 cylinder diameters. Furthermore, the size of the interrogation window meant that the velocity and vorticity fields could not be reliably computed within 0.15 diameters (one-half the interrogation window dimension) of any solid surfaces, i.e. the cylinders themselves. Hence, in the figures shown later, velocity and vorticity data are not shown in the regions very close to the cylinders. With the 75% overlap, the in-plane velocity vector field ( $57 \times 57$  vectors) and vorticity field ( $55 \times 55$  points) was resolved with a spacing of about 2.6 mm (or 0.1 cylinder diameters).

The time between successive sets of velocity or vorticity data was  $\Delta t = 0.2 \text{ s}$ . This time interval may be expressed as a fraction of the vortex shedding period  $T_s$ , determined from published data, where  $\Delta t/T_s = \Delta t^*St$  (in which  $\Delta t^* = \Delta t U/D = 0.6$ ). In these experiments,  $\Delta t$  corresponded to between 0.06 and 0.52 vortex shedding periods, depending on the configuration of the cylinders and the shedding frequency. For each configuration, eight to ten different experiments were conducted, from which a time history of the non-dimensional, instantaneous, in-plane vorticity field,  $\omega_z D/U$ , was determined. This vorticity information typically comprised eight individual fields. Given the time interval of 0.06 to 0.52 vortex shedding periods between successive instantaneous fields, sufficient information was obtained to completely represent the fluid behaviour for a complete shedding cycle. No ensemble averaging or phase averaging of data from successive runs was undertaken (nor are they possible with the given experiment set-up). In the figures and results to be presented in what follows,

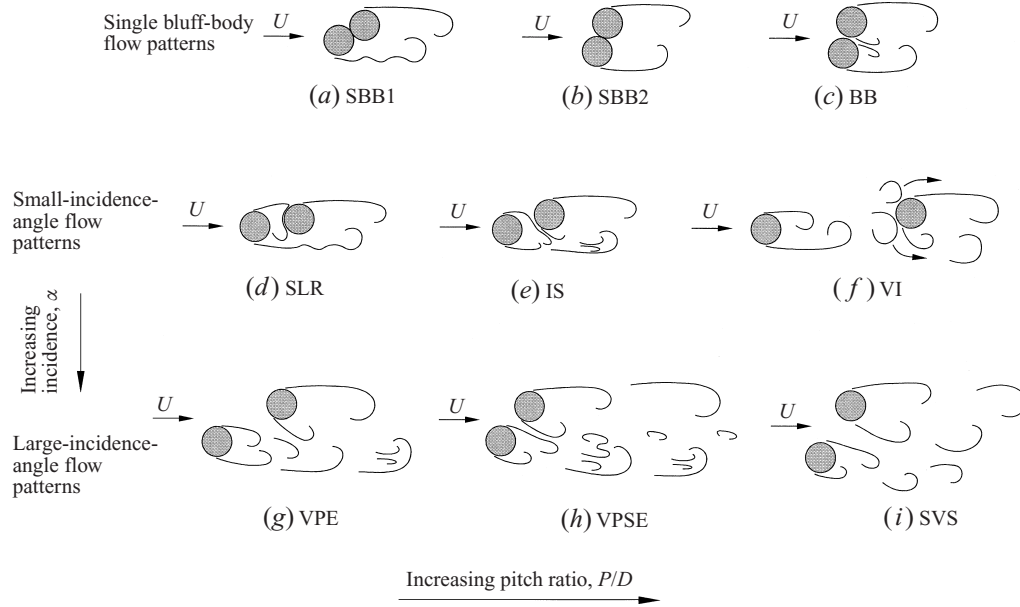


FIGURE 3. Low subcritical regime flow patterns, identified in this study, for two staggered circular cylinders of equal diameter, in steady upstream cross-flow,  $Re = 850$  to  $1900$ . Single bluff-body flow patterns: (a) type 1, SBB1; (b) type 2, SBB2; (c) base-bleed, BB. Smaller incidence flow patterns: (d) shear layer reattachment, SLR; (e) induced separation, IS; (f) vortex impingement, VI. Larger incidence flow patterns: (g) gap vortex pairing and enveloping, VPE; (h) gap vortex pairing, splitting and enveloping, VPSE; (i) synchronized gap vortex shedding, SVS.

the smallest magnitude (cut-off) contour of vorticity plotted was typically 10% to 20% of the maximum vorticity in the flow field. By applying known displacements to a digitized particle image using Adobe PhotoShop software, the measurement uncertainty of the velocity and vorticity data could be assessed; the measurement uncertainty of the vorticity was conservatively estimated at 10%.

#### 4. Overview of the flow patterns

Nine different flow patterns, shown schematically in figure 3, were identified from the flow visualization images and the instantaneous PIV vorticity data, depending on the geometrical parameters  $P/D$  and  $\alpha$ . The flow patterns cover staggered configurations of  $P/D = 1.0$  to  $5.0$ , and  $\alpha = 0^\circ$  to  $90^\circ$ , within the low subcritical regime, from  $Re = 850$  to  $1900$ . Key features of the flow patterns are summarized in table 2. They are broadly grouped into three categories: *single bluff-body flow patterns* (figure 3a–c), *flow patterns at small angles of incidence* (figure 3d–f), and *flow patterns at large angles of incidence* (figure 3g–i). There is some overlap between these categories, however, which will become clear when the flow pattern boundaries are discussed in § 8. Basic trends of increasing pitch ratio and incidence angle are also included in figure 3. The nine flow patterns from the present study are now examined in more detail.

#### 5. Single bluff-body flow patterns

When the cylinders are in contact, at  $P/D = 1.0$  (see figure 3a,b), the flow pattern resembles that of a single bluff body over the entire range of incidence angle,  $\alpha$ . The



Designation	Full name	Occurrence	Key features
SBB1	Single bluff-body, type 1	$P/D = 1.0$ to $1.125$ $\alpha = 0^\circ$ to $45^\circ$	Instabilities in the shear layer from the upstream cylinder
SBB2	Single bluff-body, type 2	$P/D = 1.0$ to $1.125$ $\alpha = 45^\circ$ to $90^\circ$	Single, low-frequency Kármán vortex shedding process
BB	Base-bleed	$P/D = 1.125$ to $1.25$ $\alpha = 45^\circ$ to $90^\circ$	Weak gap flow of variable deflection angle and a single vortex street
SLR	Shear layer reattachment	$P/D = 1.125$ to $4.0$ $\alpha = 0^\circ$ to $20^\circ$	Reattachment of the inner shear layer from the upstream cylinder
IS	Induced separation	$P/D = 1.125$ to $3.0$ $\alpha = 10^\circ$ to $30^\circ$	Narrow gap flow induces separation and vorticity generation on the inner surface of the downstream cylinder
VPE	Vortex pairing and enveloping	$P/D = 1.25$ to $3.5$ $\alpha = 20^\circ$ to $45^\circ$	Pairing of gap vortices and enveloping of the pair by a Kármán vortex from the outer shear layer of the upstream cylinder
VPSE	Vortex pairing, splitting and enveloping	$P/D = 1.25$ to $4.0$ $\alpha = 20^\circ$ to $90^\circ$	As above, but with incomplete enveloping of the gap vortex pair
SVS	Synchronized vortex shedding	$P/D = 1.5$ to $5.0$ $\alpha = 15^\circ$ to $90^\circ$	Anti-phase synchronization of gap Kármán vortex shedding
VI	Vortex impingement	$P/D = 3.0$ to $5.0$ $\alpha = 0^\circ$ to $20^\circ$	Impingement of Kármán vortices from the upstream cylinder onto the downstream cylinder

TABLE 2. Résumé of flow patterns identified in the present study for two staggered circular cylinders of equal diameter in steady cross-flow, in the low subcritical regime,  $Re = 850$  to  $1900$ . The observed ranges of pitch ratio and incidence represent the upper and lower limits for which the flow pattern is observed, and do not necessarily mean that the flow pattern will be observed for all combinations of  $P/D$  and  $\alpha$  specified.

near-wake region of the cylinder pair contains two free shear layers that alternately shed Kármán vortices at the same frequency, much like that observed for a single, isolated circular cylinder. A single Kármán vortex street, with two rows of vortices of opposite sign, is found downstream. In this study, two types of single bluff-body behaviour could be distinguished, designated SBB1 and SBB2 (figure 3*a, b*), for  $\alpha = 0^\circ$  to  $45^\circ$  and  $\alpha = 45^\circ$  to  $90^\circ$ , respectively (see figures 4 and 5). A third single bluff-body flow pattern, with the added effect of base bleed, was also observed. The base-bleed flow pattern (BB, figure 3*c*), is seen at very small pitch ratios ( $P/D = 1.0$  to  $1.25$ ) and high angles of incidence ( $\alpha = 45^\circ$  to  $90^\circ$ ). Some results are shown in figures 6 and 7.

### 5.1. Type 1 single bluff-body flow pattern (SBB1)

The type 1 single bluff-body flow pattern (SBB1, figure 3*a*) is observed at small angles of incidence. Some flow visualization images are shown in figure 4(*a–c*). PIV vorticity fields are shown in figure 5(*a, b*). For these configurations, the lengths of the two shear layers are considerably different, since the shear layer from the upstream cylinder is significantly stretched in the streamwise direction. This shear layer is prone to the development of instabilities, and regular Kármán vortex formation from this shear layer is often interrupted. The instabilities first appear as waviness in the dye streakline marking the shear layer. As the shear layer extends further from the upstream cylinder, the instabilities take on the appearance of small, Kelvin–Helmholtz

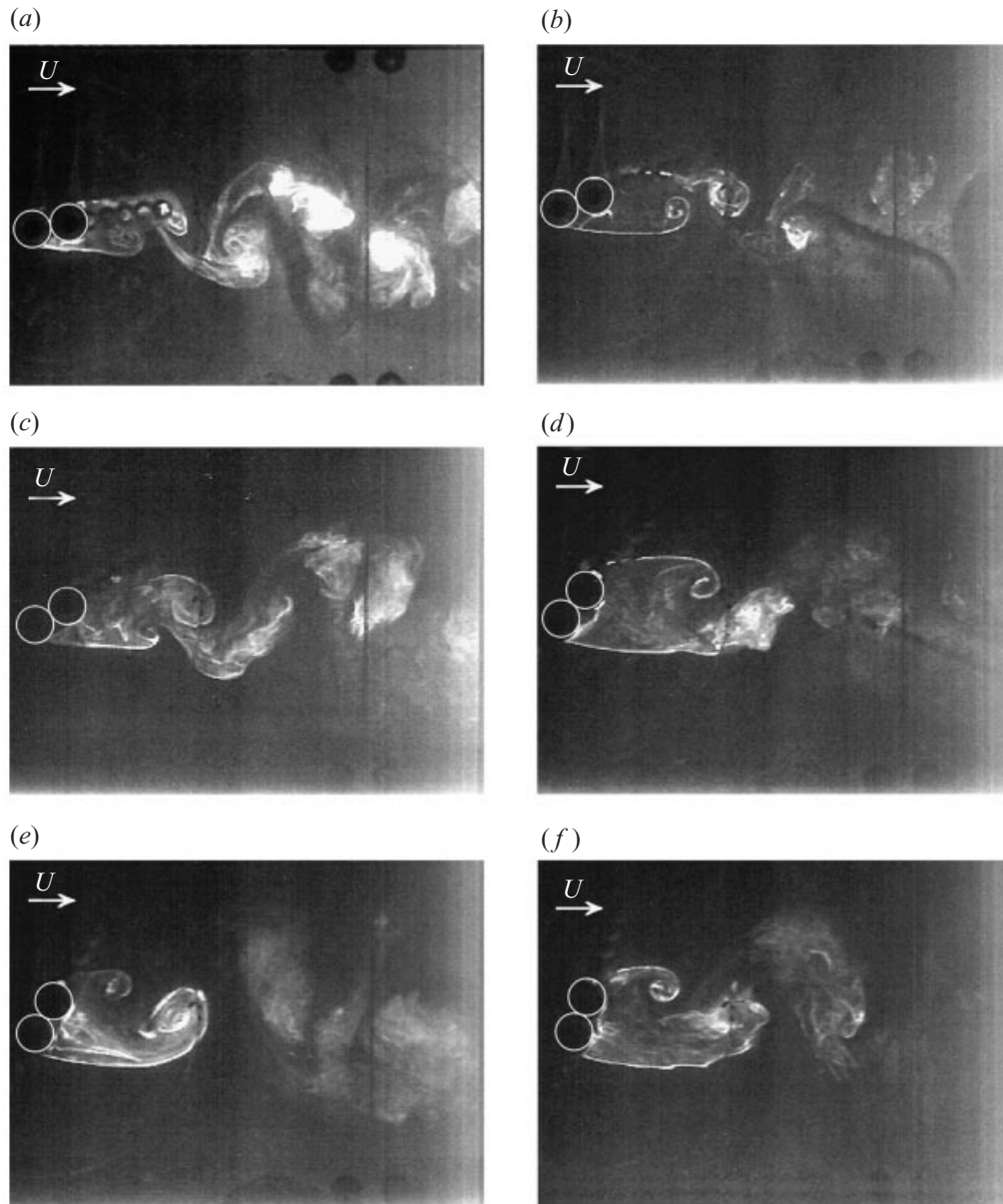


FIGURE 4. Flow visualization of single bluff-body flow patterns,  $P/D = 1.0$ . Type 1, SBB1: (a)  $\alpha = 10^\circ$ ,  $Re = 900$ ; (b)  $\alpha = 20^\circ$ ,  $Re = 1270$ ; (c)  $\alpha = 30^\circ$ ,  $Re = 1320$ . Type 2, SBB2: (d)  $\alpha = 50^\circ$ ,  $Re = 1270$ ; (e)  $\alpha = 60^\circ$ ,  $Re = 1320$ ; (f)  $\alpha = 70^\circ$ ,  $Re = 860$ .

vortices. Several of these instability vortices are then incorporated into the Kármán vortex that rolls up in the near-wake region of the cylinder pair. In contrast, the small, instability vortices are absent in the shear layer formed behind the downstream cylinder. Regular Kármán vortex shedding from the downstream cylinder is rarely interrupted, and, without the instabilities, the formation of Kármán vortices occurs without the coalescence of smaller vortical structures.

Highly stretched shear layers, such as that observed in the SBB1 pattern, are also

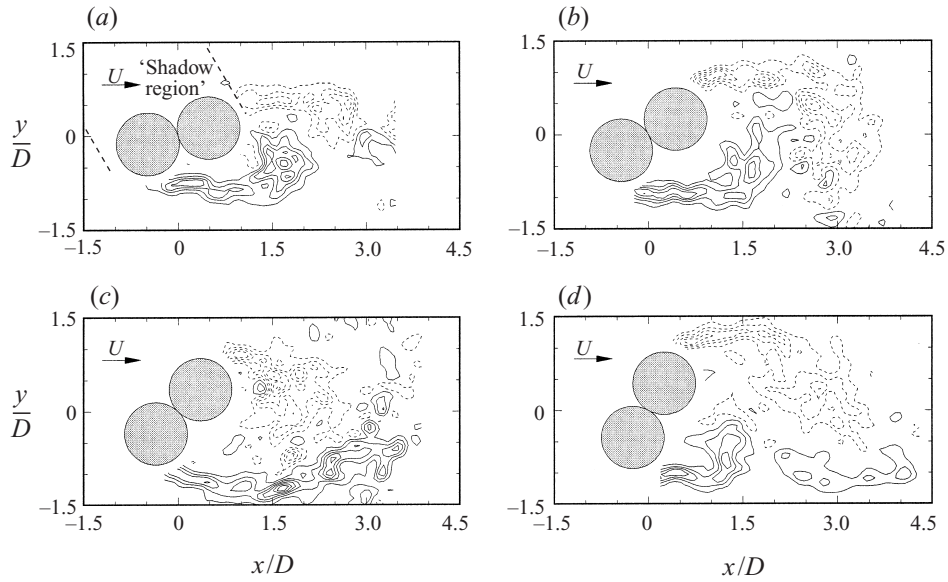


FIGURE 5. Non-dimensional, instantaneous, in-plane vorticity field for single bluff-body flow patterns,  $P/D = 1.0$ ,  $Re = 1300$ ,  $M_x = 0.25$  mm/pixel. Type 1, SBB1: (a)  $\alpha = 15^\circ$ ; (b)  $\alpha = 30^\circ$ . Type 2, SBB2: (c)  $\alpha = 45^\circ$ ; (d)  $\alpha = 60^\circ$ . Minimum vorticity contour magnitude 1.0, contour increment 1.5, solid lines represent positive (CCW) vorticity, dashed lines represent negative (CW) vorticity.

observed in the tandem configuration of cylinders, corresponding to  $\alpha = 0^\circ$ , where the two cylinders are in contact. However, in the tandem configuration, each shear layer is of the same length.

### 5.2. Type 2 single bluff-body flow pattern (SBB2)

The type 2 single bluff-body flow pattern (SBB2, figure 3b) was observed at higher angles of incidence. Examples are shown in figure 4(d–f) and figure 5(c,d). In this pattern, the streamwise lengths of the two shear layers are similar, and if instabilities are observed, they appear in both shear layers. As the angle of incidence was increased, the vortex shedding often appeared more irregular than that of a single circular cylinder. A similar result was noticed for a pair of side-by-side cylinders in contact, corresponding to  $\alpha = 90^\circ$  (Sumner *et al.* 1999). This difference, assessed on a qualitative basis, is likely to be caused by differences in the base geometry, between the cylinder pair and a larger circular cylinder of twice the diameter.

### 5.3. Base-bleed flow pattern (BB)

A third single bluff-body flow pattern can be distinguished at very large angles of incidence, for  $\alpha > 45^\circ$ , and for very small pitch ratios, for  $P/D = 1.0$  to 1.25. The base-bleed flow pattern (BB, figure 3c) is essentially a modification to the SBB2 flow pattern (§5.2), where the narrow gap permits a base-bleed flow to occur (hence it has been included with the single bluff-body flow patterns). Otherwise, the pair of cylinders resembles a single bluff-body, with a single Kármán vortex street in the combined wake (shown forming in figure 6a). This flow pattern may be seen in figures 6, 7 and 8.

The base-bleed flow pattern is similar to that observed for two side-by-side circular cylinders at small  $T/D$  (Sumner *et al.* 1999). The main effect of the narrow gap is to permit fluid to enter the base region of the cylinder pair (seen in figures 7 and

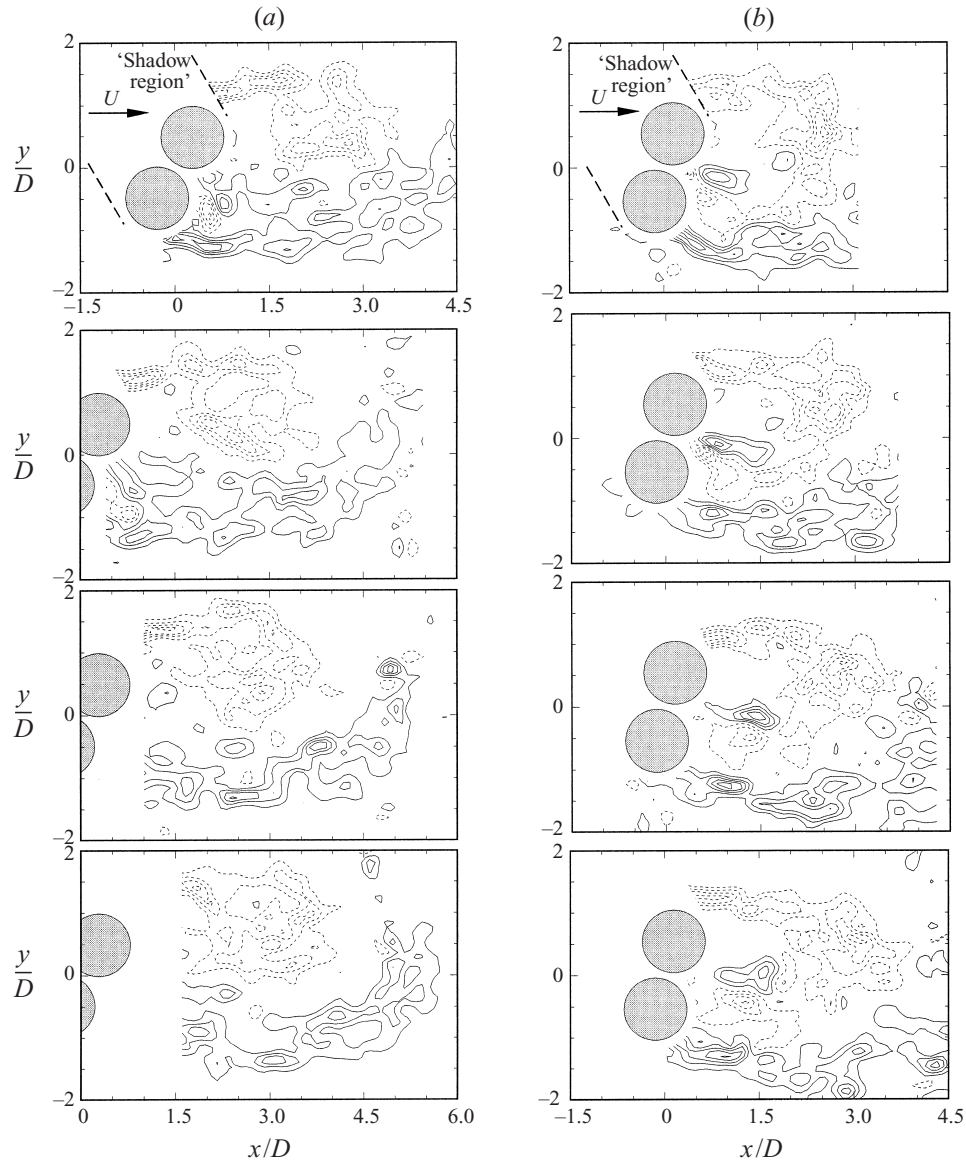


FIGURE 6. PIV vorticity data illustrating the base-bleed (BB) flow pattern,  $P/D = 1.125$ ,  $Re = 1900$ ,  $M_x = 0.25$  mm/pixel,  $\Delta t^* = 0.6$ ,  $\Delta t/T_s = 0.06$ : (a)  $\alpha = 60^\circ$ ; (b)  $\alpha = 75^\circ$ . Minimum vorticity contour magnitude 1.0, contour increment 1.5, solid lines represent positive (CCW) vorticity, dashed lines represent negative (CW) vorticity.

8), which causes a streamwise lengthening of the near-wake region and the vortex formation length, compared with the case when the two cylinders are in contact. Typically, a wider near-wake region forms behind the downstream cylinder, since the base flow is deflected away from the mean flow direction and towards the upstream cylinder (see figures 6 and 7).

The PIV data (figures 6, 7 and 8) revealed a wide variation in the vortex formation length, the base-bleed flow deflection angle, and the streamwise extent and 'strength' of the base flow. Both weak (low-magnitude) gap flow and highly deflected gap

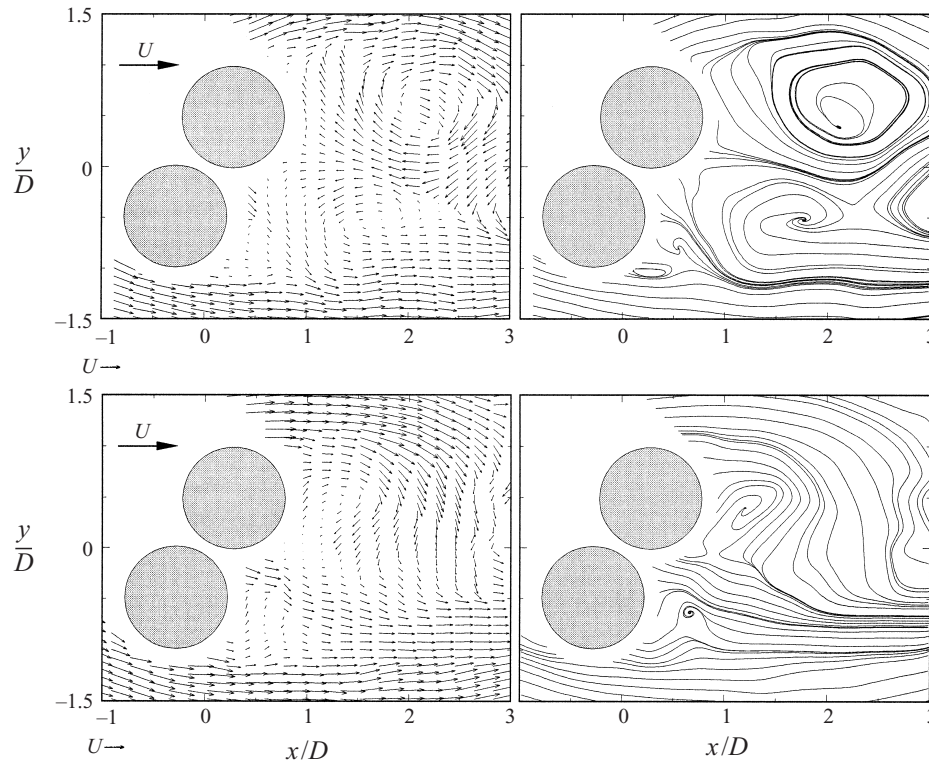


FIGURE 7. Two examples of base-bleed (BB) flow patterns,  $P/D = 1.125$ ,  $\alpha = 60^\circ$ ,  $Re = 1900$ ,  $M_x = 0.25$  mm/pixel, with a wider near-wake region behind the downstream cylinder. Instantaneous velocity fields and corresponding instantaneous streamline fields. Every second vector in the  $x$ -direction omitted for clarity. Streamlines arbitrarily chosen.

flow away from the downstream cylinder, correlated with a shorter vortex formation region, were obtained. Velocity and streamline data in figure 7 illustrate the variation in the instantaneous deflection angle for the same geometry.

Also observed for the BB flow pattern was reverse gap flow deflection, where the base-bleed flow is deflected instantaneously towards the downstream cylinder; see figure 8. This unique result yields a wider near wake behind the upstream cylinder. The existence of reverse gap flow deflection is supported by Zdravkovich (1987), for nearly side-by-side configurations, provided  $-0.15 < L/D < 0.15$ ; in this same range of  $L/D$ , the deflection was found to be bistable, intermittently deflecting from one cylinder to the other. The BB flow patterns in the present study had  $L/D = 0.3$  to  $0.6$ , which is much higher than the range given by Zdravkovich (1987); this may simply be a result of the instantaneous nature of the PIV data.

## 6. Flow patterns at small angles of incidence

At small angles of incidence, from  $\alpha = 0^\circ$  to  $45^\circ$ , flow through the gap between the cylinders and vortex shedding from the upstream cylinder are mostly suppressed, except at large pitch ratios. Three flow patterns were identified within this range of incidence angle, as described in the following sections, and shown in figures 9 and 10. It is within this range of incidence that some of the more interesting lift and



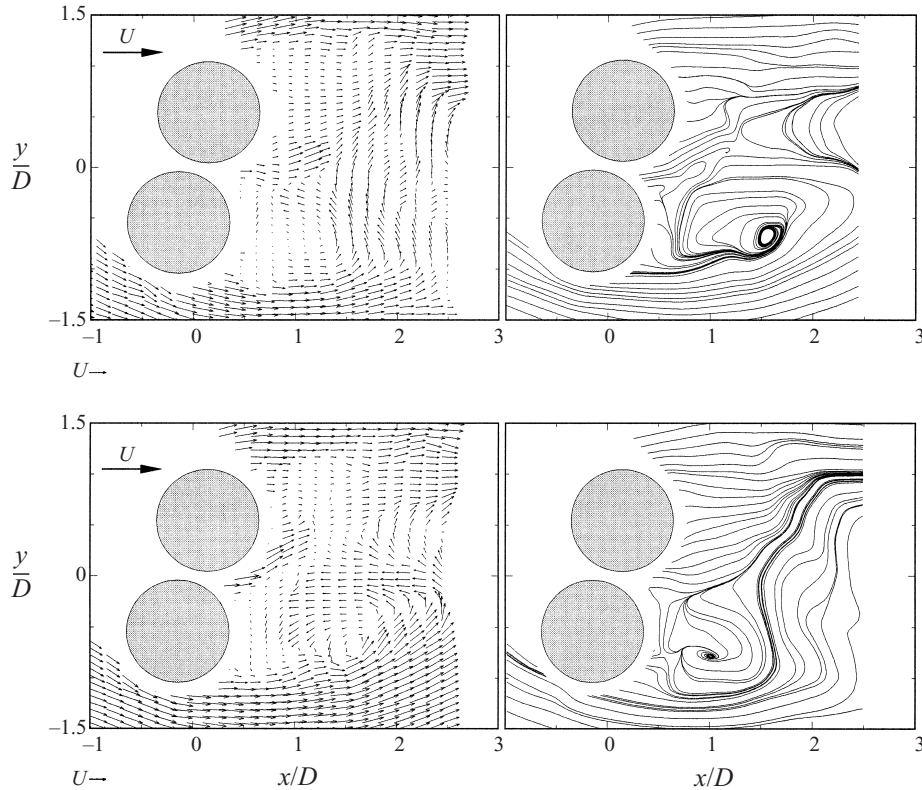


FIGURE 8. Two examples of base-bleed (BB) flow patterns,  $P/D = 1.125$ ,  $\alpha = 75^\circ$ ,  $Re = 1900$ ,  $M_x = 0.21$  mm/pixel, with a wider near-wake region behind the upstream cylinder. Instantaneous velocity fields and corresponding instantaneous streamline fields. Every second vector in the  $x$ -direction omitted for clarity. Streamlines arbitrarily chosen.

drag force changes have been observed by other researchers, in the upper subcritical regime (Zdravkovich & Pridden 1977; Ting *et al.* 1998).

#### 6.1. Shear layer reattachment flow pattern (SLR)

For very small pitch ratios,  $P/D < 3.0$ , and at small angles of incidence,  $\alpha < 10^\circ$  to  $20^\circ$ , the shear layer reattachment flow pattern (SLR, figure 3d) is observed. The flow is not substantially different from the single bluff-body case, described in § 5.1 (the SBB1 pattern, specifically); see figures 9(a,b) and 10(a-c). Although there is now a gap between the two cylinders, flow through the gap is prevented by the formation of a separated shear layer from the inside surface of the upstream cylinder. This shear layer reattaches onto the outer surface of the cylinder immediately downstream (figures 9a,b and 10a-c, which effectively prevents the oncoming mean flow from penetrating the gap between the cylinders; this is more clearly seen in the streamline plots, found in figure 10(b,c), for geometries with positive ( $\alpha = +5^\circ$ ) and negative stagger ( $\alpha = -5^\circ$ ), respectively. Consequently, the structure of the combined wake remains essentially the same as the SBB1 flow pattern (§ 5.1, figure 3a), with a single Kármán vortex street (and Strouhal number) in the combined wake of the cylinder pair. As with the SBB1 flow pattern, the outer shear layer of the upstream cylinder remains highly stretched in the streamwise direction, and is prone to the same waviness and instability vortices. Consequently, the periodic, alternate vortex shedding process

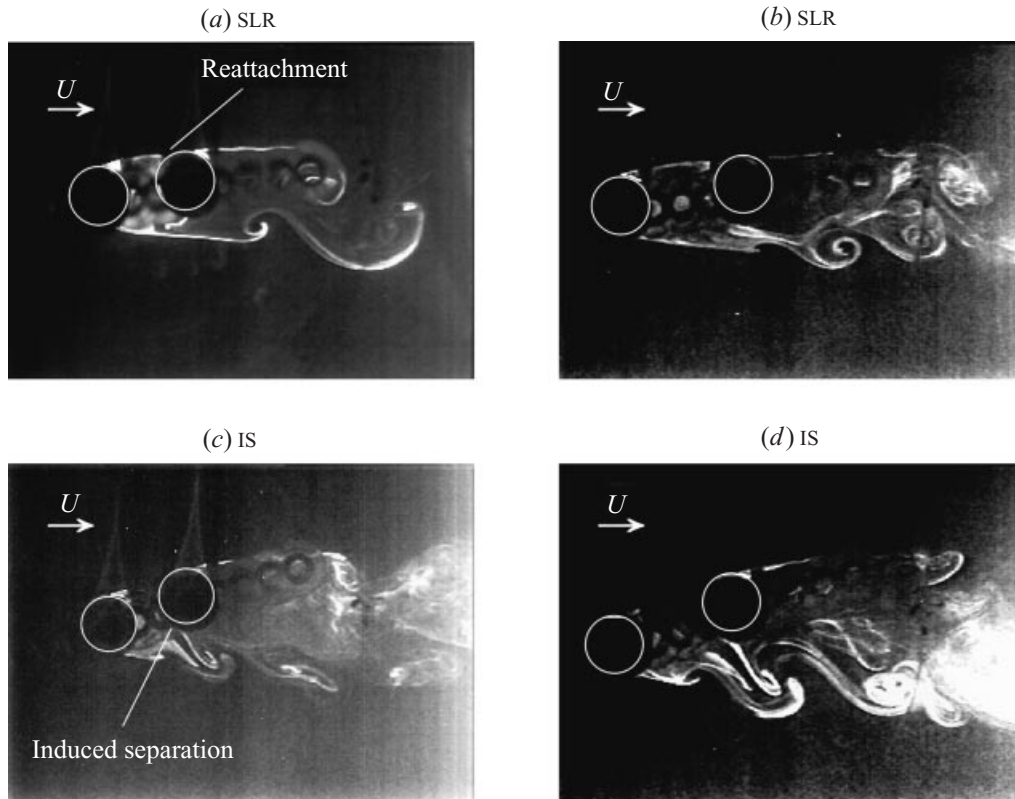


FIGURE 9. Flow visualization of small-incidence-angle staggered configurations. SLR flow pattern: (a)  $P/D = 1.5$ ,  $\alpha = 10^\circ$ ,  $Re = 1300$ ; (b)  $P/D = 2.0$ ,  $\alpha = 10^\circ$ ,  $Re = 880$ . IS flow pattern: (c)  $P/D = 1.5$ ,  $\alpha = 20^\circ$ ,  $Re = 1320$ ; (d)  $P/D = 2.0$ ,  $\alpha = 20^\circ$ ,  $Re = 850$ .

is often interrupted, particularly from the stretched shear layer from the upstream cylinder.

Gu & Sun (1999) made similar observations for a staggered pair of cylinders in the high subcritical regime (denoted therein as 'Pattern I<sub>B</sub>' for the downstream cylinder). The SLR flow pattern may be distinguished in the flow visualization results of Ishigai *et al.* (1972), at  $L/D = 2.0$ ,  $T/D = 0.5$  ( $P/D = 2.06$ ,  $\alpha = 14^\circ$ ), and  $Re = 1690$ . However, no systematic identification of flow patterns was undertaken in that work. Shear layer reattachment is also found in triangular and square clusters of three and four cylinders, particularly under conditions of 'fully-shielded' flow (Lam & Cheung 1988; Lam & Lo 1993).

Through analysis of the flow visualization videos, the shear layer reattachment process was observed to be a steady phenomenon. Steady (as opposed to unsteady or periodic) reattachment was observed for triangular and square clusters of circular cylinders at incidence, by Lam & Cheung (1988) and Lam & Lo (1993), in the same range of low subcritical Reynolds number. In contrast, shear layer reattachment for a tandem configuration of cylinders, where  $\alpha = 0^\circ$ , occurs in an alternating, periodic fashion, in synchronization with Kármán vortex shedding from the downstream cylinder (Igarashi 1981, 1984; Sumner 1999). Synchronized, alternating shear layer reattachment is thus unique to the tandem configuration. This may be explained from a stability viewpoint, by considering the tandem arrangement as a

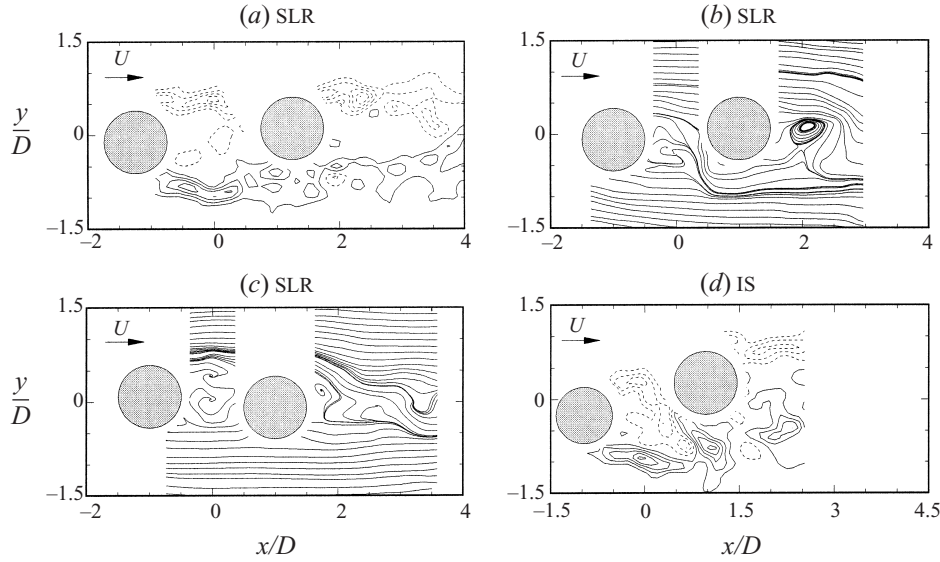


FIGURE 10. PIV data illustrating flow patterns at small angles of incidence,  $Re = 1900$ . Shear layer reattachment (SLR) flow pattern: (a) vorticity field,  $P/D = 2.5$ ,  $\alpha = 5^\circ$ ,  $M_x = 0.25$  mm/pixel; (b) streamline field,  $P/D = 2.0$ ,  $\alpha = +5^\circ$ ,  $M_x = 0.21$  mm/pixel; (c) streamline field,  $P/D = 2.0$ ,  $\alpha = -5^\circ$ ,  $M_x = 0.21$  mm/pixel. Induced separation (IS) flow pattern: (d)  $P/D = 2.0$ ,  $\alpha = 15^\circ$ ,  $M_x = 0.25$  mm/pixel. Minimum vorticity contour magnitude 1.0, contour increment 1.5, solid lines represent positive (CCW) vorticity, dashed lines represent negative (CW) vorticity. Streamlines arbitrarily chosen.

critical cylinder geometry between staggered configurations of positive and negative incidence.

Within the interstitial region, bounded by the reattached shear layer on one side, and by the free shear layer from the upstream cylinder on the opposite side, the flow visualization images (figure 9a, b) show mostly stagnant fluid in the gap between the cylinders. This conclusion is supported by the PIV data (figure 10a), which show very low levels of vorticity between the cylinders. No organized fluid motion, in the form of a pair of eddies for example, was observed, as has been suggested (without convincing proof) in a number of studies of the tandem configuration (see Igarashi 1981, 1984, and others).

### 6.2. Induced separation flow pattern (IS)

At slightly greater angles of incidence, from  $\alpha = 10^\circ$  to  $30^\circ$ , but for a similar range of  $P/D$  as the SLR flow pattern (§6.1), shear layer reattachment can no longer be maintained (see figures 9c, d and 10d). The induced separation flow pattern (IS, figure 3e) is now observed. Here, the downstream cylinder is now situated further away from the flow axis of the upstream cylinder, and it is now easier for the inner shear layer from the upstream cylinder to be deflected into the gap between the cylinders. In addition, some of the oncoming mean flow is now permitted to penetrate the gap between the cylinders.

This gap flow effectively signals the end of the stretched shear layer from the outside of the upstream cylinder. In its place, a small near-wake region forms behind the upstream cylinder (figures 9c, d and 10d); this small region is highly constrained within the gap between the cylinders, and is biased away from the downstream cylinder and



the flow axis. Each of the shear layers bounding the near-wake region rolls up in an alternating, periodic fashion, into small-diameter Kármán vortices. The frequency of vortex formation is higher than that of a single circular cylinder.

The Kármán vortices from the inner shear layer, however, form very close to the surface of the downstream cylinder, and induce a separation of the flow from this cylinder. Production of vorticity about the second cylinder accompanies the separated flow. The IS flow pattern may also be discerned from the results of Ishigai *et al.* (1972), for a staggered configuration of  $L/D = 1.0$ ,  $T/D = 0.5$  ( $P/D = 1.12$ ,  $\alpha = 27^\circ$ ), at  $Re = 2560$ . This pattern is consistent with that identified for a pair of staggered cylinders in the high subcritical regime, by Gu & Sun (1999), and denoted therein as 'Pattern II<sub>B</sub>'.

The flow visualization videos show that the induced, separated flow (or generated vorticity) on the downstream cylinder is not steady. Rather, the induced separation is periodic, at the same frequency as the Kármán vortex shedding from the upstream cylinder. A pairing of vorticity of opposite sign is noticed across the gap, but the paired vorticity is enveloped by a vortex from the outer shear layer of the upstream cylinder, to form a single larger composite vortex (figure 9*d*). Within the pair, the dominant vorticity is that induced on the surface of the downstream cylinder (figure 10*d*).

The induced separation and vorticity production on the inner surface of the downstream cylinder is distinct from Kármán vortex formation, since it does not involve the formation and roll-up of a free shear layer. It is similar to the vorticity generation due to a vortex impinging upon another body in its path, as in the case of the vortex impingement (VI) flow pattern identified for two staggered cylinders (§6.3, figure 3*f*). Similar induced separation and vorticity formation is also seen in the second row of cylinders for a normal triangular array (Oengören & Ziada 1995), particularly for arrays with small pitch ratios. In the array, the induced vortex formation from cylinders in the second row is distinct from Kármán vortex shedding, in that no free shear layers are involved. Rather, the induced formation is caused by the Kármán vortices shed from cylinders in the first row, as they are squeezed around cylinders in the second row. The induced vortex formation occurs at the same frequency as Kármán shedding from upstream cylinders, and pairing of vorticity of opposite sign is seen just beyond the second row.

The combined wake of the cylinder group remains similar to that for the type 1 single bluff-body (SBB1, §5.1) and shear layer reattachment (SLR, §6.1) flow patterns, with two rows of Kármán vortices. However, the frequencies of Kármán vortex formation are different for each row, since those formed from the outer shear layer of the downstream cylinder are considerably lower. This difference in the rate of vortex formation, found in the combined wake of the cylinder pair, is an important flow feature of the staggered configuration for a wide range of  $P/D$  and  $\alpha$ .

### 6.3. Vortex impingement flow pattern (VI)

At large pitch ratios and small angles of incidence, shear layer reattachment on the downstream cylinder can no longer be maintained, given the distance over which the shear layer must remain thin and stable. Once the pitch ratio reaches  $P/D = 3.0$  or 4.0, the inner shear layer from the upstream cylinder begins to periodically roll up into Kármán vortices, and the shear layer reattachment (SLR, §6.1) flow pattern is no longer observed.

A further consequence of increasing the distance between the cylinders is that the spatial development of the near-wake region behind the upstream cylinder is no longer constrained. Consequently, the induced separation (IS, §6.2) flow pattern is no

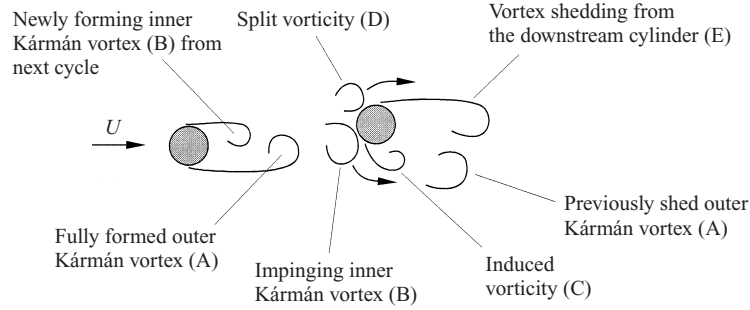


FIGURE 11. The vortex impingement (VI) flow pattern for two staggered circular cylinders in cross-flow. A – Kármán vortex from the outer shear layer of the upstream cylinder, B – Kármán vortex from the inner shear layer of the upstream cylinder, C – induced vorticity on the downstream cylinder, D – vorticity concentration split upon vortex impingement, E – Kármán vortex from the outer shear layer of the downstream cylinder.

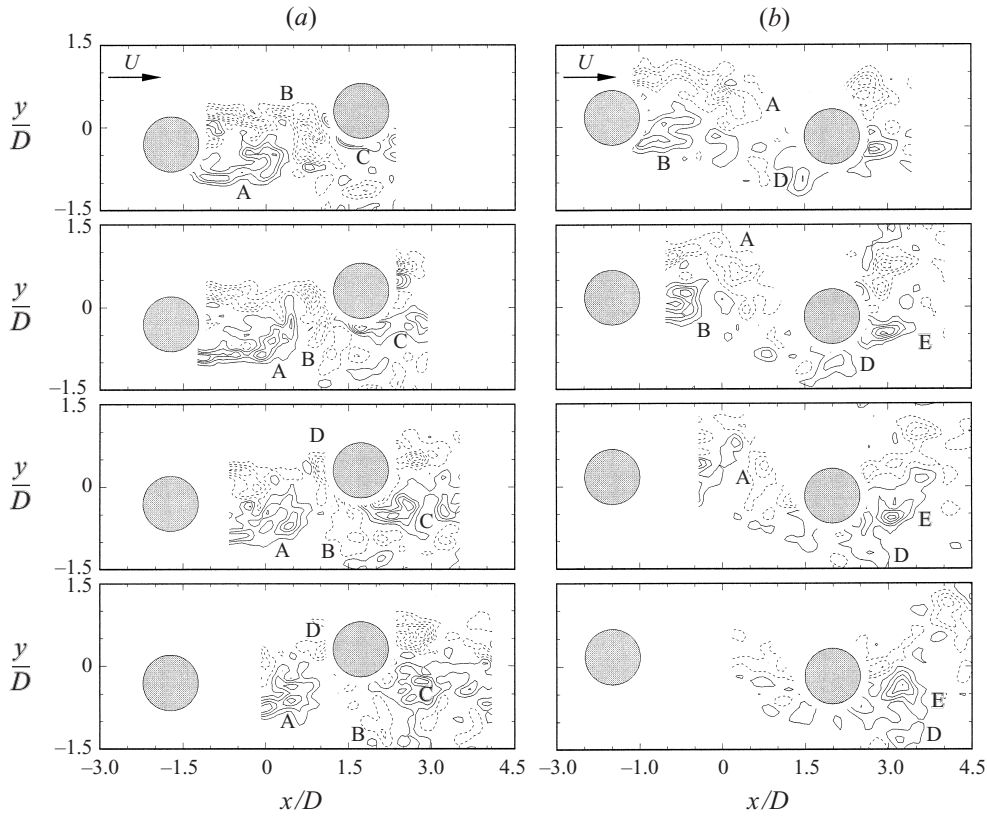


FIGURE 12. Vorticity data for the VI flow pattern,  $Re = 1900$ ,  $\Delta t^* = 0.6$ : (a)  $P/D = 3.5$ ,  $\alpha = 10^\circ$ ,  $M_x = 0.22$  mm/pixel,  $\Delta t/T_s = 0.11$ ; (b)  $P/D = 4.0$ ,  $\alpha = -5^\circ$ ,  $M_x = 0.25$  mm/pixel,  $\Delta t/T_s = 0.10$ ; (c)  $P/D = 4.0$ ,  $\alpha = 15^\circ$ ,  $M_x = 0.25$  mm/pixel,  $\Delta t/T_s = 0.11$ ; (d)  $P/D = 4.0$ ,  $\alpha = 15^\circ$ ,  $M_x = 0.25$  mm/pixel,  $\Delta t/T_s = 0.11$ . Minimum vorticity contour magnitude 1.0, contour increment 1.5, solid lines represent positive (CCW) vorticity, dashed lines represent negative (CW) vorticity. For labels A–E see figure 11 caption.

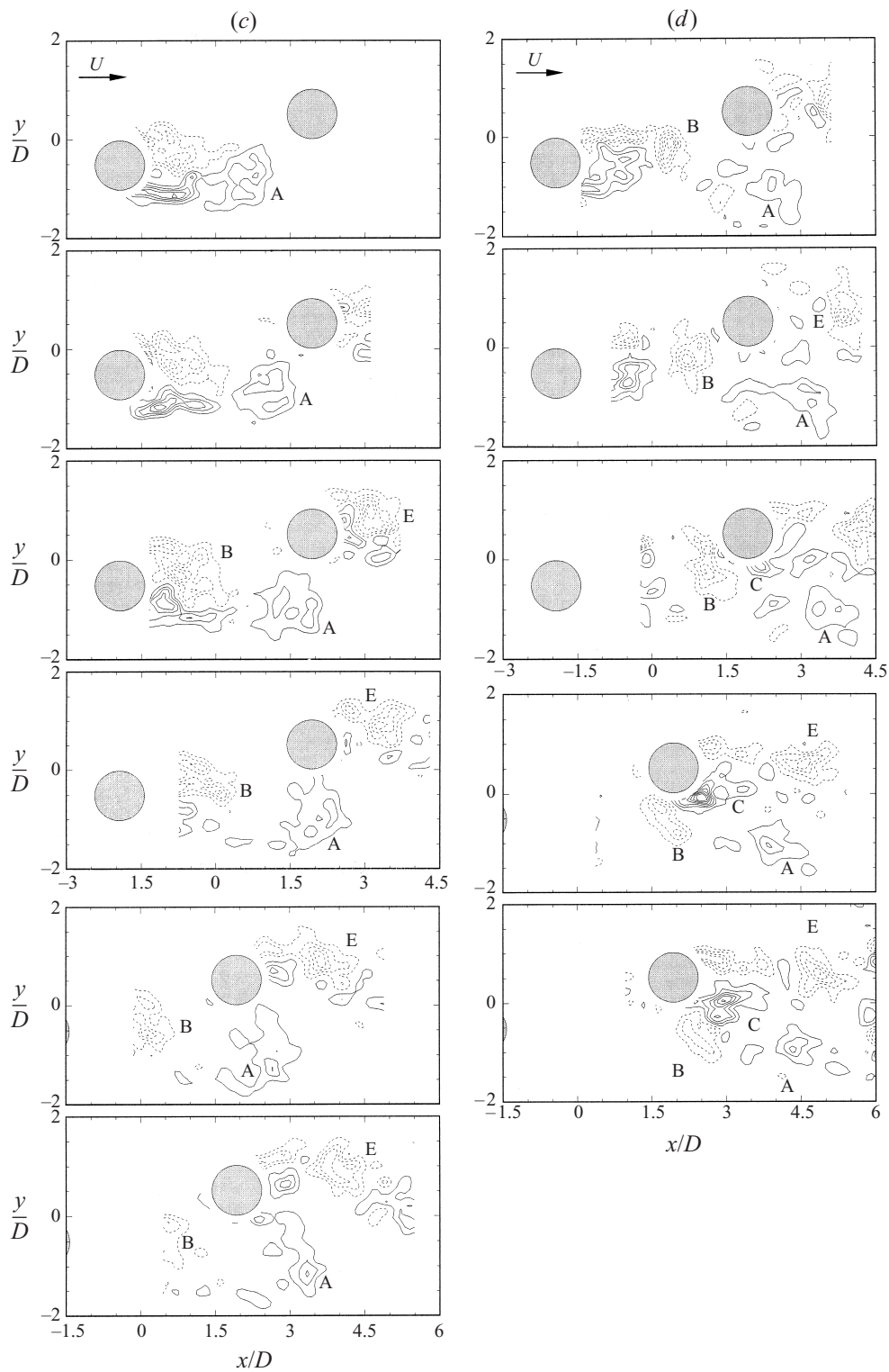


FIGURE 12(c,d). For caption see facing page.

longer observed either, since the downstream cylinder is now sufficiently far removed. The near-wake region of the upstream cylinder can now form uninhibited, similar to a single, isolated circular cylinder.

The result, for small angles of incidence, is unbiased, alternate Kármán vortex shedding from the upstream cylinder, at a frequency close to that of a single circular cylinder. The Kármán vortices shed from the upstream cylinder impinge upon the downstream one, hence the vortex impingement flow pattern arises (VI, figure 3*f*). The VI flow pattern may also be distinguished in the flow visualization results of Ishigai *et al.* (1972), for a geometry of  $L/D = 4.0$ ,  $T/D = 1.0$  ( $P/D = 4.12$ ,  $\alpha = 14^\circ$ ) and  $Re = 2790$ .

The VI flow pattern is shown schematically in figure 11, where the main features include the incident Kármán vortices shed from the upstream cylinder (labelled A and B), induced vorticity about the downstream cylinder (labelled C), split vorticity (labelled D), and Kármán vortex shedding from the downstream cylinder (labelled E).

These features may be identified in the PIV vorticity data shown in figure 12. In the present experiments, two different types of vortex impingement behaviour were identified, depending on whether one or two rows of Kármán vortices impinged on the downstream cylinder, as illustrated in figure 12.

Where two rows of vortices impinge on the downstream cylinder, vortices from the inner row (labelled B in figure 12*a, b*) are split into two concentrations of vorticity during the impingement process (labelled B and D in figure 12*a, b*). Each portion is convected around the downstream cylinder and induces vorticity in its near-wake region (labelled C). In figure 12(*b*), the split vorticity (D) that is convected about the outside of the downstream cylinder is entrained into the newly forming Kármán vortex (E).

Where only one row of vortices impinges on the downstream cylinder, Kármán vortices shed from the outer shear layer of the upstream cylinder (A) will remain intact (figure 12*c*). As these vortices convect past the downstream cylinder, they become strained and distorted. Opposite-sign vorticity is not induced, however. Vortices shed from the inner shear layer (B), which impinge upon the downstream cylinder, continue to split into two concentrations of vorticity (figure 12*d*). Opposite-sign vorticity is induced about the second cylinder in this case (labelled C).

Vortex shedding from the downstream cylinder is highly disturbed by the impingement of the vortex street from upstream. Consequently, it is very difficult to observe. The Strouhal number data measured in the wakes of the upstream and downstream cylinders show the same frequency. This may indicate synchronization between the impingement flow and Kármán vortex shedding from the downstream cylinder, analogous to a lock-in condition (Rockwell 1998); however, this could not be verified in the present study.

The interaction between a vortex street and the body in its path is, according to Gursul & Rockwell (1990), primarily influenced by two parameters. These parameters are: (i) the relative scales of the vortex street and the body, denoted by the streamwise spacing of the Kármán vortices in one row of the vortex street,  $l$ , and (in this case) the cylinder diameter,  $D$ , expressed as the dimensionless ratio  $l/D$ ; and (ii) the transverse offset of the vortex street centreline from the centre of the body, which in the case of two staggered cylinders corresponds to the value of the transverse pitch ratio,  $T/D$ . In the present case, the ratio  $l/D = 4.0$  is taken from vortex shedding experiments for a single cylinder (Sumner 1999). The three staggered configurations shown in figure 12, of  $P/D = 3.5, \alpha = 10^\circ$  (figure 12*a*),  $P/D = 4.0, \alpha = -5^\circ$  (figure 12*b*), and  $P/D = 4.0, \alpha = 15^\circ$  (figure 12*c, d*), correspond to  $T/D = 0.61, 0.35$ , and  $1.04$ ,

respectively. Based on the study of Gursul & Rockwell (1990), for  $l/D = 4.0$  the flow pattern referred to here as the VI pattern corresponds to a 'large-scale' vortex street, and the configurations in figure 12 correspond to the second and third types of interaction mechanisms identified by Gursul & Rockwell (1990), where either one or two rows of Kármán vortices are disturbed.

In the tandem case, the axis of the Kármán vortex street from the upstream cylinder is aligned with the centre of the cylinder downstream, and both rows of vortices impinge symmetrically on the downstream cylinder. These vortices become highly strained and distorted, and induce vorticity of opposite sign in the near wake of the downstream cylinder (Sumner 1999). Considering the staggered case, as shown in figure 12, a VI flow pattern with impingement of two rows of vortices is shown in figure 12(a,b), and with one row of vortices in figure 12(c,d). In both cases, the PIV vorticity data show induced vorticity generated about the second cylinder (labelled C in figures 11 and 12), caused by an impinging vortex, and rapid deformation of the impinging vortices.

One finding of practical importance for the vortex impingement (VI) flow pattern is that the vortex-body interaction will cause large changes in the time-dependent pressure forces and loading on the downstream cylinder (Gursul & Rockwell 1990; Rockwell 1998), and hence will significantly affect the r.m.s. values of the fluid force coefficients acting on the downstream cylinder. Such a phenomenon is important in the study of flow-induced vibrations of multiple cylinder systems (Rockwell 1998).

## 7. Flow patterns at larger angles of incidence

At larger angles of incidence, from  $\alpha = 30^\circ$  to  $90^\circ$ , a portion of the oncoming mean flow is always permitted to enter the gap between the two cylinders (figures 13 and 14). Vortex shedding now occurs from each of the cylinders, for all the flow patterns at higher angles of incidence. The flow patterns at higher angles of incidence appear as evolutions of the induced separation (IS, §6.2) flow pattern.

Vortex shedding from each cylinder occurs for two reasons. First, the angle of incidence is now sufficiently high that the inner shear layer from the upstream cylinder no longer reattaches onto the downstream cylinder; consequently, the shear layer reattachment (SLR, §6.1) flow pattern is not observed. Second, the potential for vortex impingement decreases at larger angles of incidence,  $\alpha$ , since the downstream cylinder is situated further from the flow axis of the upstream cylinder. For  $\alpha > 20^\circ$ , for example, the VI flow pattern (§6.3) found at large pitch ratios is no longer observed.

### 7.1. Synchronized vortex shedding flow pattern (SVS)

The most commonly observed flow pattern for the staggered configuration is one of synchronized vortex shedding (SVS, figure 3i). It is observed at higher angles of incidence,  $\alpha = 20^\circ$  to  $90^\circ$ , and for a wide range of pitch ratios,  $P/D > 1.5$  (figures 13a–c and 14a,b). The near-field flow pattern is marked by flow through the gap between the cylinders, which is deflected away from the flow axis, resulting in two different widths of near-wake regions, and two dominant frequencies of vortex shedding. Still within the near field, vortex shedding on either side of the gap flow becomes synchronized. Vortices of opposite sign, from opposite sides of the gap, are observed to pair up. Within the combined wake of the pair of cylinders, this results in two adjacent Kármán vortex streets that exhibit anti-phase synchronization. The flow pattern is similar to that for two side-by-side circular cylinders, at intermediate

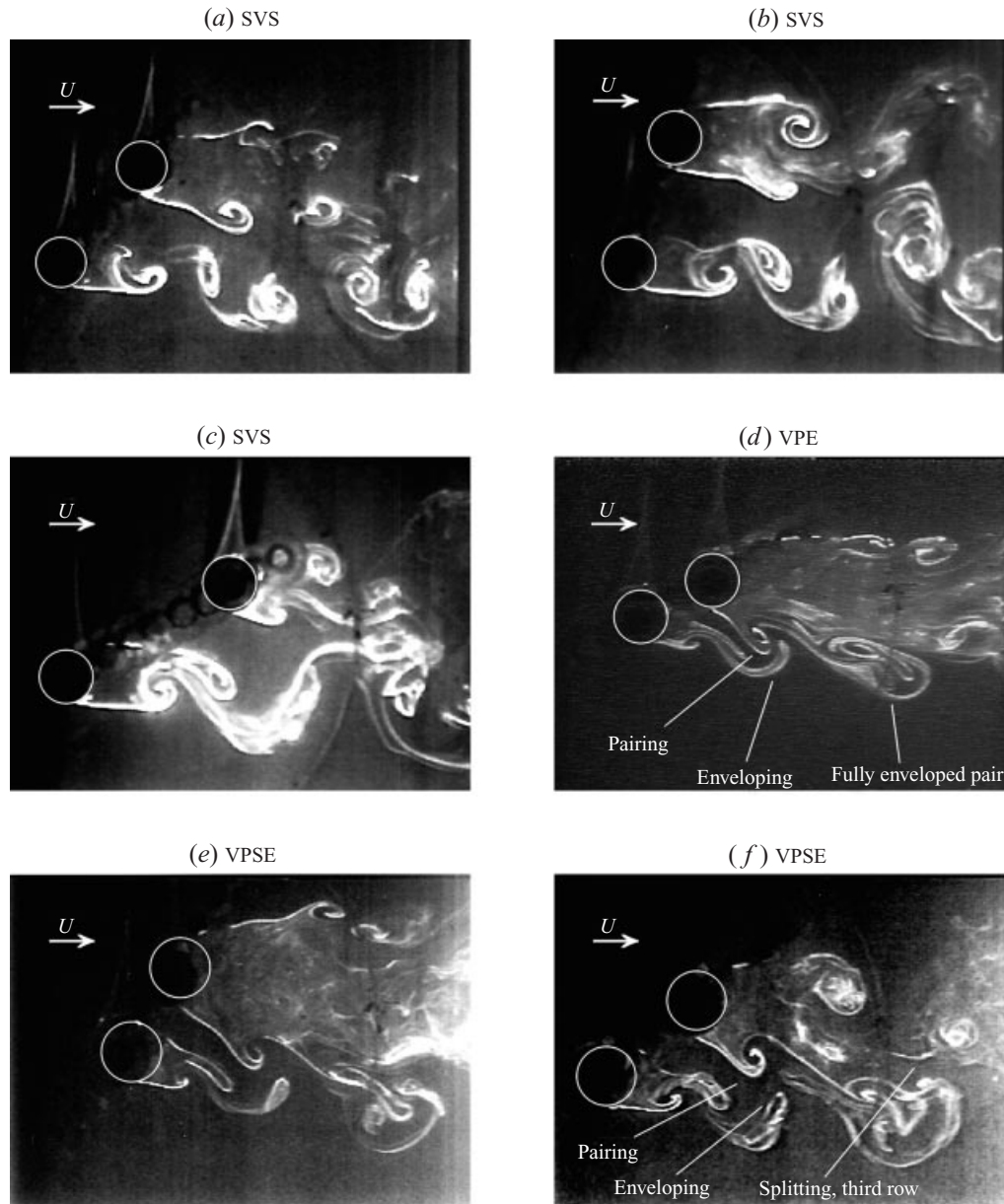


FIGURE 13. Flow visualization of large-incidence staggered configurations. SVS flow pattern: (a)  $P/D = 2.5$ ,  $\alpha = 50^\circ$ ,  $Re = 900$ ; (b)  $P/D = 2.5$ ,  $\alpha = 70^\circ$ ,  $Re = 900$ ; (c)  $P/D = 3.5$ ,  $\alpha = 30^\circ$ ,  $Re = 830$ . VPE flow pattern: (d)  $P/D = 1.5$ ,  $\alpha = 30^\circ$ ,  $Re = 850$ . VPSE flow pattern: (e)  $P/D = 1.5$ ,  $\alpha = 60^\circ$ ,  $Re = 900$ ; (f)  $P/D = 2.0$ ,  $\alpha = 40^\circ$ ,  $Re = 880$ .

and large  $T/D$  (Sumner *et al.* 1999). This behaviour is an evolution of the gap vortex pairing phenomenon, first seen in the induced separation (IS, §6.2, figure 3e) flow pattern, but also seen in the VPE and VPSE flow patterns still to be described (§7.2, figure 3g, h).

Some more specific details are now highlighted. As shown in figures 13(a–c) and 14(a, b), strong interaction occurs between the two shear layers on either side of

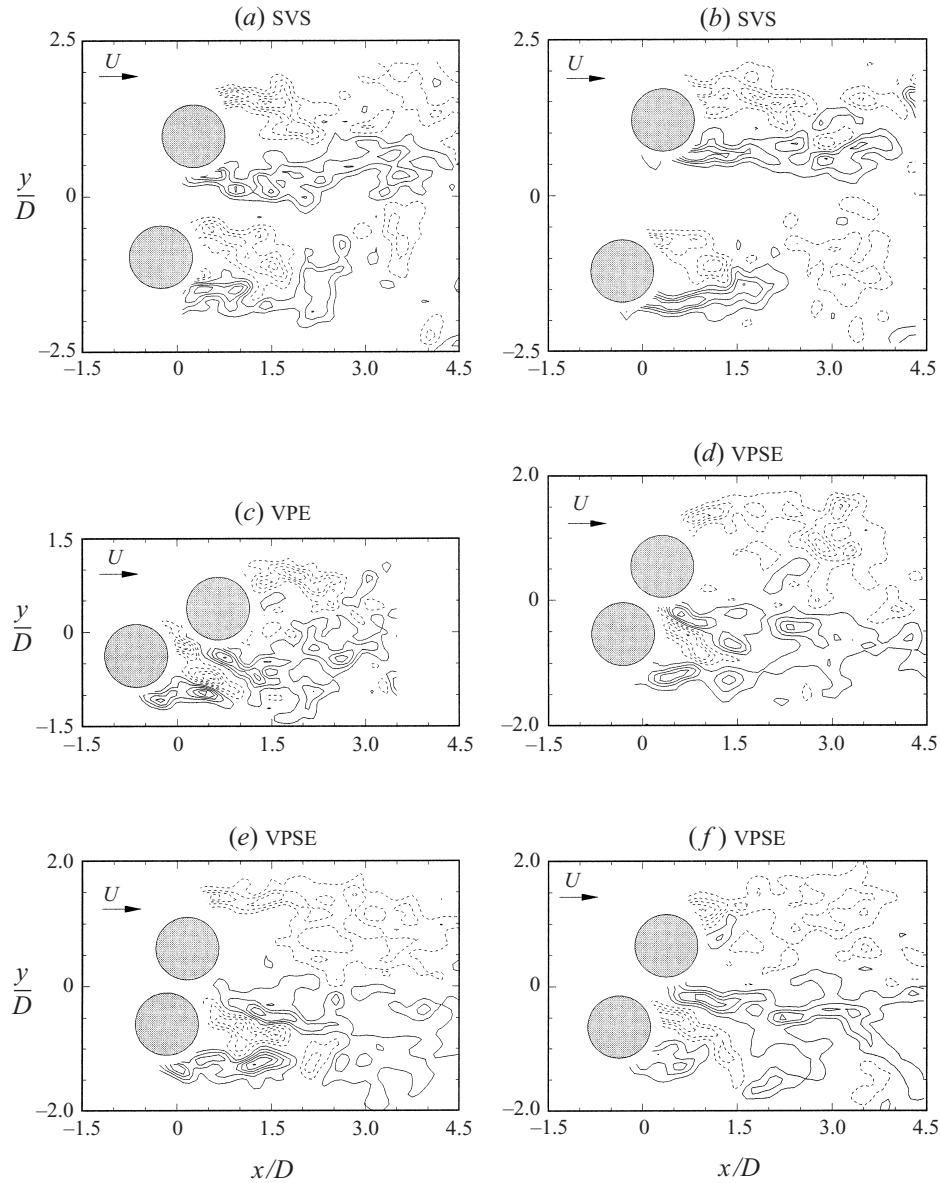


FIGURE 14. PIV vorticity data illustrating flow patterns at high angles of incidence,  $Re = 1900$ . SVS flow pattern: (a)  $P/D = 2.0$ ,  $\alpha = 75^\circ$ ,  $M_x = 0.25$  mm/pixel; (b)  $P/D = 2.5$ ,  $\alpha = 75^\circ$ ,  $M_x = 0.25$  mm/pixel. VPE flow pattern: (c)  $P/D = 1.5$ ,  $\alpha = 30^\circ$ ,  $M_x = 0.21$  mm/pixel. VPSE flow pattern: (d)  $P/D = 1.25$ ,  $\alpha = 60^\circ$ ,  $M_x = 0.25$  mm/pixel; (e)  $P/D = 1.25$ ,  $\alpha = 75^\circ$ ,  $M_x = 0.25$  mm/pixel; (f)  $P/D = 1.5$ ,  $\alpha = 60^\circ$ ,  $M_x = 0.25$  mm/pixel. Minimum vorticity contour magnitude 1.0, contour increment 1.5, solid lines represent positive (CCW) vorticity, dashed lines represent negative (CW) vorticity.

the gap, along with simultaneous shedding of Kármán vortices from the gap at the same frequency. Pairing of vortices across the gap, during their formation, is seen at smaller  $P/D$  in figures 13(a,b) and 14(a,b). Pairing of gap vortices at larger  $P/D$  often occurs far downstream from the upstream cylinder, as shown in figure 13(c). In each case, this pairing of vortices across the gap occurs at some distance apart, and

a counter-rotating vortex pair structure is not formed. The two side-by-side vortex streets may be seen in figure 13(*b, c*), synchronized in an anti-phase manner.

As in many of the other staggered flow patterns, vortex shedding frequencies are mostly unique for each individual shear layer rather than for each cylinder (see figure 1*b*). In most but not all SVS configurations, the two shear layers from the upstream cylinder and the inner shear layer from the downstream cylinder shed vortices at the same frequency. Lower-frequency Kármán shedding then occurs from the fourth shear layer only, from the outer side of the downstream cylinder; these larger vortices may be seen forming in figure 13(*b*). The difference in shedding frequency across the near wake of the downstream cylinder may be discerned from the symmetric vortex formation shown in figure 13(*a*), and from the irregular vortex street behind this cylinder. High-frequency modulation of the low-frequency vortex formation, denoted by interruptions to its regular shedding behaviour, may be seen by the pairs of outer vortices in figure 13(*a*), or irregular vortex patterns behind the downstream cylinder (not shown).

For SVS configurations of larger  $P/D$  and larger  $\alpha$ , however, both shear layers from the downstream cylinder are more inclined to shed vortices at the same, lower frequency, with reduced high-frequency modulation. This may mean that a subdivision of the SVS flow pattern is needed, but extensive vortex shedding frequency measurements with a hot-film anemometer, positioned in each of the shear layers, would be required to verify the frequency relationship.

### 7.2. Vortex pairing and enveloping flow patterns (VPE, VPSE)

At smaller pitch ratios, the gap flow for the higher-incidence cylinder pairs is appreciably narrower, and the near-wake region behind the upstream cylinder is more constrained and distorted (figures 13*d–f* and 14*c–f*). The shear layers on either side of the gap, and the Kármán vortices formed from them, now are more closely and strongly synchronized. The gap vortices also form at much closer proximity to one another. The synchronization remains the same in terms of frequency, as it did in the synchronized vortex shedding (SVS, §7.1) flow pattern, with vortices on either side of the gap forming at the same rate and at the same time. However, the pairing of vortices of opposite sign across the gap results in a counter-rotating vortex pair structure at the gap exit, which is then enveloped by a Kármán vortex from the outer shear layer of the upstream cylinder; see figure 15.

When making a distinction between this new pattern and the SVS pattern (described in §7.1), it is the counter-rotating vortex pair structure, and the existence of the enveloping process, which mark the new fluid behaviour at the smaller pitch ratios. This pairing and enveloping action is not unique to the staggered configuration, however. Similar behaviour was observed for three side-by-side cylinders, at  $T/D = 1.5$  (Sumner 1999; Sumner *et al.* 1999), and in the first harmonic mode of vortex shedding for two side-by-side cylinders (Williamson 1985).

From the flow visualization videos, two flow patterns involving this type of pairing and enveloping phenomenon could be distinguished (figure 15). The first pattern involves complete enveloping of the gap-vortex pair, designated as the ‘vortex pairing and enveloping’ flow pattern (VPE, figures 3*g* and 15*a*). This flow pattern is marked by two rows of vortices in the combined wake of the cylinders (figures 13*d* and 14*c*). A second pattern with incomplete enveloping, involving splitting of the vortex pair, is designated as the ‘vortex pairing, splitting and enveloping’ flow pattern (VPSE, figures 3*h* and 15*b*). Examples are provided in figures 13(*e, f*) and 14(*d–f*). The flow visualization results of Ishigai *et al.* (1972) for configurations of  $L/D = 0.68$ ,  $T/D =$



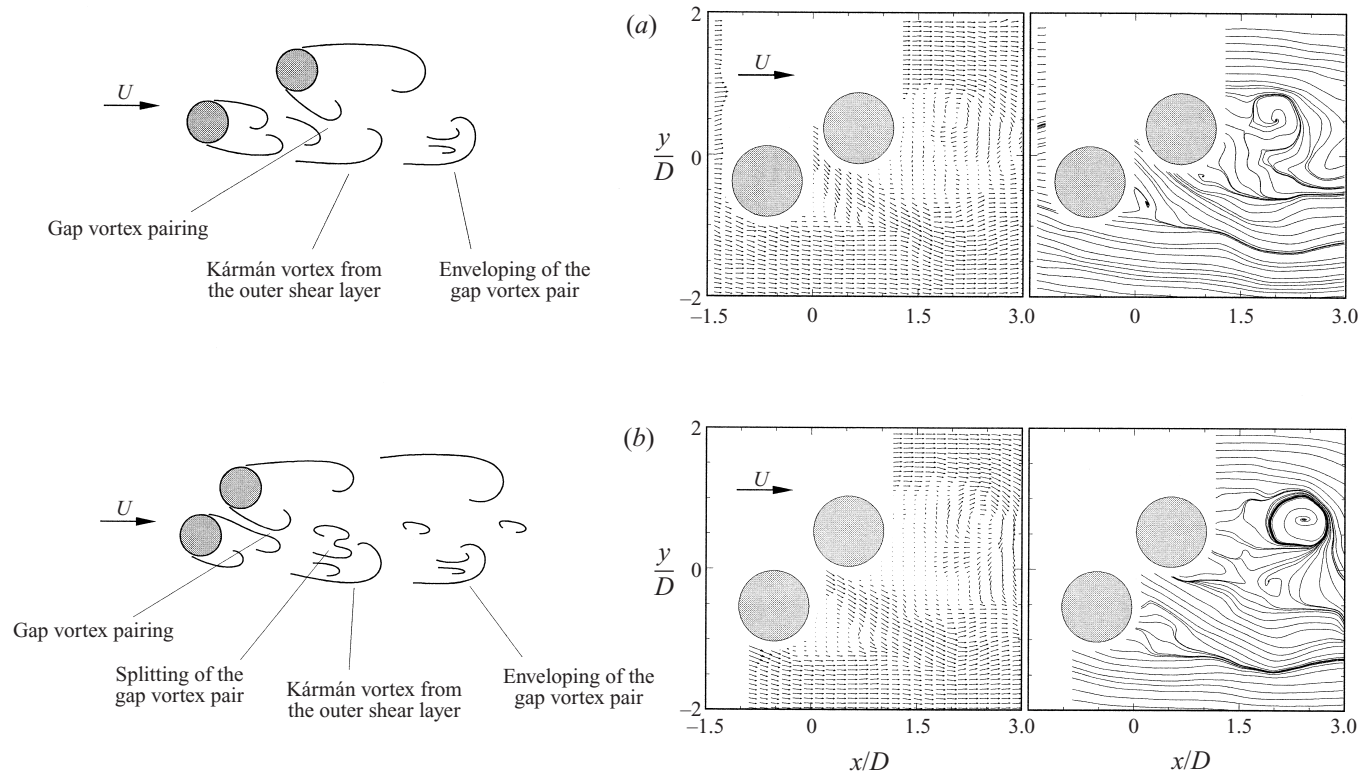


FIGURE 15. Staggered cylinder flow patterns with gap vortex pairing. (a) VPE flow pattern, with complete enveloping of the gap vortex pair by an outer vortex from the upstream cylinder. Instantaneous velocity and instantaneous streamline data for  $P/D = 1.5$ ,  $\alpha = 30^\circ$ ,  $Re = 1900$ ,  $M_x = 0.21$  mm/pixel. (b) VPSE flow pattern, with incomplete enveloping and splitting of the gap vortex pair, during the enveloping process. Instantaneous velocity and instantaneous streamline data for  $P/D = 1.5$ ,  $\alpha = 45^\circ$ ,  $Re = 1900$ ,  $M_x = 0.21$  mm/pixel. Every second velocity vector in the x-direction omitted for clarity. Streamlines arbitrarily chosen.

1.0 ( $P/D = 1.21$ ,  $\alpha = 34^\circ$ ), at  $Re = 1600$ ;  $L/D = 1.0$ ,  $T/D = 1.0$  ( $P/D = 1.4$ ,  $\alpha = 45^\circ$ ), at  $Re = 2140$ ; and  $L/D = 2.0$ ,  $T/D = 1.0$  ( $P/D = 2.24$ ,  $\alpha = 27^\circ$ ), at  $Re = 3500$ , would broadly correspond to the VPSE flow pattern; however, the pairing, splitting, or enveloping processes cannot be clearly distinguished in their photographs. A flow pattern designated by Gu & Sun (1999) as 'Pattern III<sub>B</sub>', for the staggered configuration in the high subcritical regime, would also be consistent with VPE and VPSE activity.

The more prevalent of the two gap vortex pairing and enveloping flow patterns is the VPSE pattern (figure 15*b*), in which the enveloping process is incomplete. Because of the greater distance between the gap shear layers, and the Kármán vortices formed from them, each inner gap vortex splits into two concentrations of vorticity during the enveloping process. The split vorticity typically forms a third row of smaller vortices in the combined wake of the cylinders, which may be seen in figure 13(*f*), and as a concentration of vorticity parallel to the flow axis in figure 14(*f*). The combined wake of the cylinder pair then contains three rows of vortices, with two rows of like-sign vortices behind the upstream cylinder; these two like-sign vortex rows represent an unstable arrangement, however.

In both the VPE and VPSE flow, as demonstrated by the video recordings, three of the four shear layers and their associated vortex formation and shedding process have the same high frequency of vortex shedding. This contrasts with the traditional understanding of the staggered configuration, which implies that high- and low-frequency vortex shedding are associated with individual cylinders, rather than with individual shear layers. The two different frequencies of vortex shedding mean that the combined wake of the cylinders contains an irregular street of two rows of vortices. The low-frequency shedding from the outer shear layer of the downstream cylinder was often modulated by the high-frequency vortex shedding occurring elsewhere. When this modulation occurred, the low-frequency shedding was interrupted (see figure 13*e*, for example); this often meant that two subsequent Kármán vortices combined to form a composite vortex.

As the angle of incidence is increased within the VPE flow pattern, the gap flow becomes less deflected, and enveloping occurs further downstream. Eventually, if the angle of incidence becomes sufficiently high, or the pitch ratio becomes sufficiently great, there is a transition to the synchronized vortex shedding (SVS, § 7.1, figure 3*i*) flow pattern. If the pitch ratio is reduced, meaning the cylinders are positioned closer together, Kármán vortex formation is suppressed from the inner shear layer of the downstream cylinder, and the IS flow pattern (§ 6.2, figure 3*e*) results.

### 7.3. Vortex strength measurements

The most reliable and extensive measurements of vortex strength (or circulation),  $\Gamma$ , were obtained for the synchronized vortex shedding (SVS, § 7.1) flow pattern, since vortices from each of the four different shear layers could easily be identified. In other flow patterns, such as VPE and VPSE (§ 7.2), vortices from the upstream cylinder could not always be clearly identified from the instantaneous PIV vorticity data. Vortices were designated as belonging to the upstream or downstream cylinder, and as being shed from the inside (adjacent to the gap) or the outside (adjacent to the mean flow) of the staggered configuration. Measurements of vortex strength for the downstream cylinder were acquired in limited numbers, for two reasons: (*a*) the field of view of the digital camera was not always sufficiently large to image beyond the vortex formation region of the downstream cylinder; (*b*) these vortices are formed

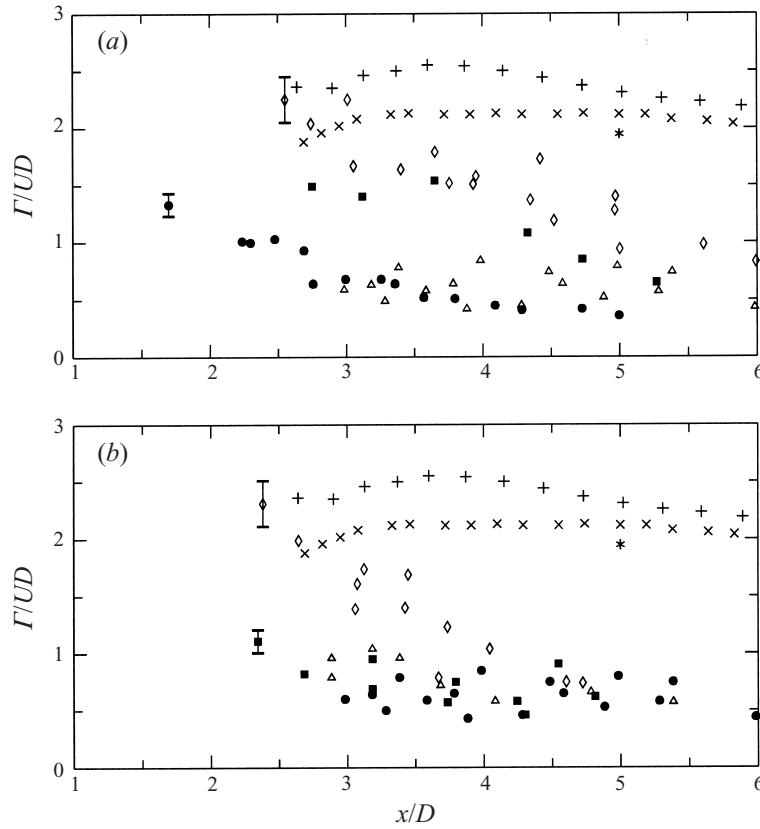


FIGURE 16. Strength of Kármán vortices shed from the inner shear layer of the upstream cylinder, for a two-cylinder staggered configuration in steady upstream cross-flow, SVS flow pattern,  $Re = 1900$ , vorticity cutoff magnitude 1.5. (a) Constant incidence of  $\alpha = 30^\circ$ :  $\bullet$ ,  $P/D = 2.0$ ;  $\triangle$ ,  $P/D = 2.5$ ;  $\blacksquare$ ,  $P/D = 3.0$ ;  $\diamond$ ,  $P/D = 4.0$ ; (b) Constant pitch ratio of  $P/D = 2.5$ :  $\bullet$ ,  $\alpha = 30^\circ$ ;  $\triangle$ ,  $\alpha = 45^\circ$ ;  $\blacksquare$ ,  $\alpha = 60^\circ$ ;  $\diamond$ ,  $\alpha = 75^\circ$ . Streamwise coordinate  $x/D$  measured from the different cylinder centres, and not from the centre of the configuration. Single circular cylinder data: \*, Schmidt & Tilmann (1972),  $Re = 5100$ ;  $\times$ , Tanaka & Murata (1986),  $Re = 37\,000$ ;  $+$ , Cantwell & Coles (1983),  $Re = 140\,000$ . Measurement uncertainty estimated at 10%; representative error bars shown.

at much lower frequencies than those from the upstream cylinder. The measurement uncertainty of the vortex strength is estimated at  $\pm 10\%$ .

Some results for vortex strength are shown in figures 16 and 17, plotted against the streamwise distance,  $x/D$ , from the centre of each cylinder, rather than from the centre of the staggered configuration. The vortex strength data presented in figures 16 and 17 were chosen for specific staggered configurations that best illustrate trends seen consistently throughout the complete SVS data set, the complete data set being too large to present here.

The circulation values given are not meant to be absolute; the purpose here is to illustrate basic trends in the vortex strength for the SVS flow pattern. Nonetheless, comparison is made with published vortex strength measurements for a single circular cylinder. Data acquired by Schmidt & Tilmann (1972) at  $Re = 5100$ , Tanaka & Murata (1986) at  $Re = 37\,000$ , and Cantwell & Coles (1983) at  $Re = 140\,000$ , listed here in order of increasing Reynolds number, are also plotted in figures 16 and 17. These data were acquired at Reynolds numbers considerably higher than that in the

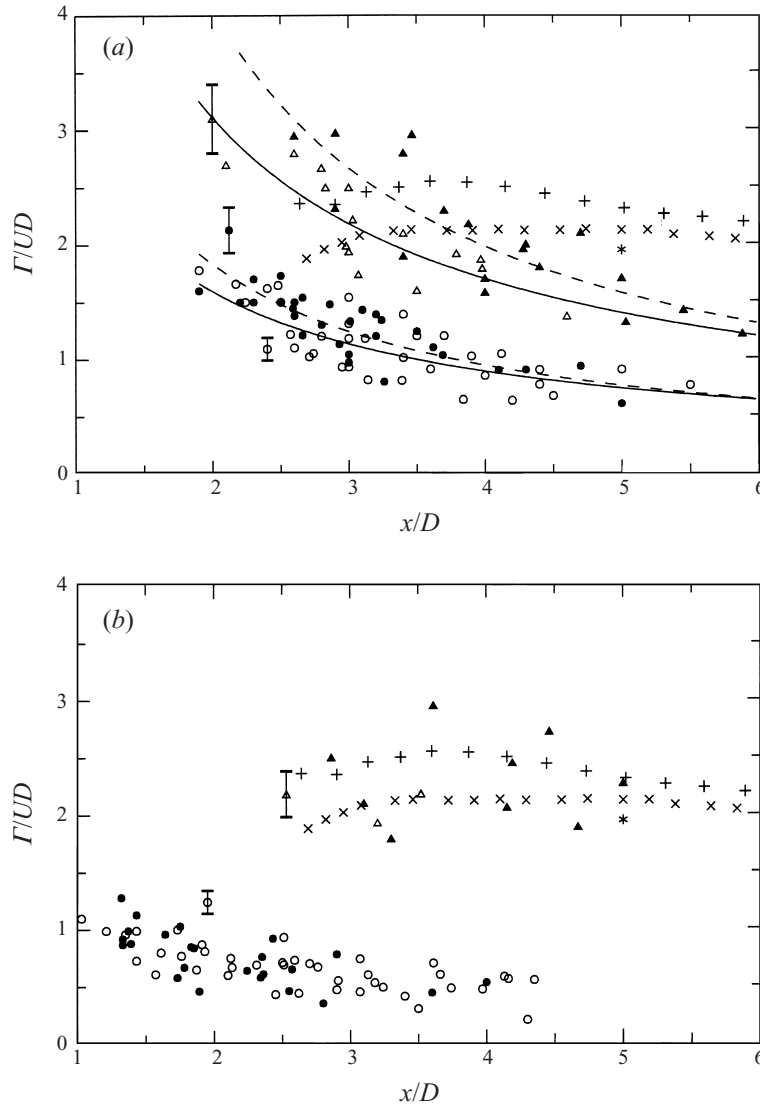


FIGURE 17. Kármán vortex strength measurements for two staggered cylinders in steady cross-flow, SVS flow pattern,  $P/D = 2.0$ ,  $Re = 1900$ , vorticity cutoff magnitude 1.5: (a)  $\alpha = 75^\circ$ ; (b)  $\alpha = 45^\circ$ . Upstream cylinder:  $\circ$ , inner vortices;  $\bullet$ , outer vortices. Downstream cylinder:  $\triangle$ , inner vortices;  $\blacktriangle$ , outer vortices. Power-law curve fit lines shown for illustration purposes only: solid lines, inner vortices; dashed lines, outer vortices. Streamwise coordinate  $x/D$  measured from the different cylinder centres, and not from the centre of the configuration. Single circular cylinder data: \*, Schmidt & Tilmann (1972),  $Re = 5100$ ;  $\times$ , Tanaka & Murata (1986),  $Re = 37\,000$ ;  $+$ , Cantwell & Coles (1983),  $Re = 140\,000$ . Measurement uncertainty estimated at 10%; representative error bars shown.

current study ( $Re = 1900$ ); however there is a general trend toward lower vortex strength measurements with decreasing Reynolds number. Differences in circulation values between the individual single-cylinder studies may also be attributed to different measurement and phase-averaging techniques, as well as the spatial resolutions of the different measuring systems.

The results in both figures 16 and 17 illustrate a power-law decay in strength with streamwise distance from the centres of the cylinders. This decay is independent of  $P/D$ ,  $\alpha$ , the cylinder, or the shear layer. Although the decay rate for the staggered cylinder data is more rapid than that of the single cylinder data, this is expected given the interference of the cylinders and their vortex streets.

In figure 16(a), the effects of varying  $P/D$  at constant  $\alpha$  are illustrated for Kármán vortices shed from the inner shear layer from the upstream cylinder. Results are given for  $\alpha = 30^\circ$ , and show an increase in strength as the spacing between the cylinders is increased from  $P/D = 2.0$  to 4.0. This increase in strength is proportional to the width and size of the near-wake region behind the downstream cylinder, which expands as the downstream cylinder is positioned further away. As the pitch ratio is increased, the strengths of these vortices (from the inner shear layer of the upstream cylinder) slowly approach that of the single circular cylinder. This indicates that no-interference conditions are established for  $P/D > 4.0$ , and there is no more anti-phase synchronization of the two vortex streets. Conversely, the lower values of the circulation at smaller pitch ratios reflect the higher interference conditions. The lower values are attributed to cancellation of opposite-sign vorticity between adjacent vortex streets, the increasingly narrower near-wake region behind the upstream cylinder, and a transition from the SVS pattern to the VPSE pattern with a further reduction in  $P/D$ .

In figure 16(b) the effects of varying  $\alpha$  at constant  $P/D = 2.5$  are illustrated, again for vortices shed from the inner shear layer of the upstream cylinder. Increasing  $\alpha$  has the same effect as increasing  $P/D$ , producing an increase in the vortex strength. In both cases, the increase in vortex strength is caused by reduced interference of the second cylinder, and less distortion of the near-wake region behind the upstream cylinder. In this case, however, the circulation values do not rapidly approach the single cylinder data with an increase in the incidence angle, as in the previous case at constant incidence (figure 16a). This is because interference, in the form of anti-phase synchronized vortex shedding, continues to exist up to  $\alpha = 90^\circ$ , which corresponds to the side-by-side configuration (Sumner *et al.* 1999). Anti-phase synchronization of the two adjacent vortex streets means there will be cancellation of opposite-sign vorticity across the gap between the cylinders, causing a reduction in the vortex strength.

In figure 17, the strengths of the Kármán vortices from the inner and outer shear layers of both cylinders are compared. Data are given for two SVS flow patterns for: (a)  $P/D = 2.0$  and  $\alpha = 75^\circ$ , and (b)  $P/D = 2.0$  and  $\alpha = 45^\circ$ . A corresponding vorticity field for the  $P/D = 2.0, \alpha = 75^\circ$  case, of figure 17(a), was shown in figure 14(a). These circulation measurements illustrate two common trends. First, Kármán vortices shed from the downstream cylinder are usually higher in strength than those shed from the upstream cylinder. Furthermore, the strengths of the vortices shed from the downstream cylinder are consistent with those shed from a single isolated circular cylinder, also shown in figure 17. Second, Kármán vortices shed from outer shear layers are more often of greater strength than those shed from inner shear layers (see figure 17a, in particular). Since the vortices are shed in a symmetric fashion across the gap, and pair in an anti-phase manner between the two parallel vortex streets, it might be expected that the inner Kármán vortices are weaker than those on the outside, due to cancellation of opposite-sign vorticity. This trend was not consistently observed for all the SVS configurations, however. For example, vortex strength data from small incidence SVS configurations typically showed no difference in circulation between inner and outer vortices from the upstream cylinder, as shown by the data in figure 17(b). This figure also shows that the difference in strength between the

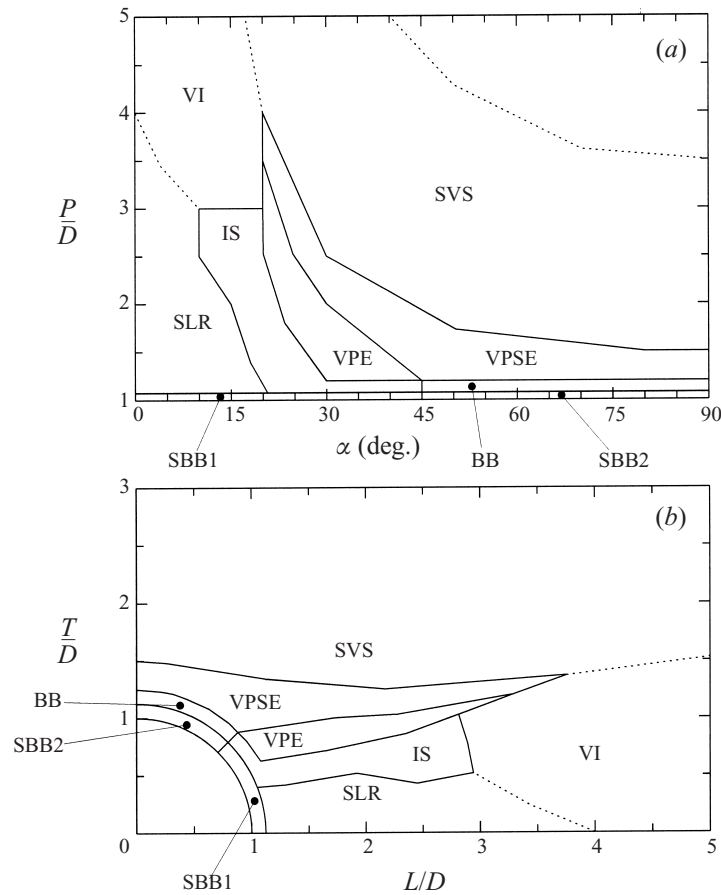


FIGURE 18. Flow pattern boundaries for two staggered cylinders in steady upstream cross-flow, in the low subcritical regime,  $Re = 850$  to  $1900$ : (a)  $P/D$ – $\alpha$  notation; (b)  $L/D$ – $T/D$  notation. BB, base-bleed; IS, induced separation; SBB1, single bluff-body type 1; SBB2, single bluff-body type 2; SLR, shear layer reattachment; SVS, synchronized vortex shedding; VI, vortex impingement; VPE, gap vortex pairing and enveloping; VPSE, gap vortex pairing, splitting and enveloping. Dotted lines represent proposed boundaries.

Kármán vortices shed from the upstream and downstream cylinders decreases as  $\alpha$  is increased (or for that matter, as  $P/D$  is increased, at constant  $\alpha$ ).

## 8. Flow pattern boundaries

Based on the flow visualization and PIV experiments, approximate boundaries for the nine distinct flow patterns were drawn. These are shown in figure 18 for the two different types of notation,  $P/D$  versus  $\alpha$ , and  $L/D$  versus  $T/D$ . For the tandem configuration, similar flow pattern diagrams were produced by Igarashi (1981, 1984) and Ljungkrona (1992), based on  $L/D$  and the Reynolds number.

In regions where limited experiments were undertaken (see figure 2), the extent of the flow patterns was difficult to assess, and the suggested boundaries are marked with dotted lines in figure 18. The boundaries do not mean that a sudden transition always occurs from one flow pattern to another. An abrupt transition may be noticed between the shear layer reattachment (SLR) and induced separation (IS) flow patterns,

for example, where the oncoming flow is suddenly deflected through the inter-cylinder gap. However, in most cases the change is gradual, and two flow patterns alternate in an irregular or intermittent fashion for configurations close to a boundary. Similar behaviour is seen in the case of two tandem cylinders, in the changeover from shear layer reattachment to Kármán vortex shedding from the upstream cylinder (Igarashi 1981, 1984; Ljungkrona 1992). In addition, there may be an actual transitional flow pattern not seen in the present study because of the limited number of experiments.

### 8.1. Reynolds number effects

The experiments on which figure 18 is based were conducted for a limited range of Reynolds number, from  $Re = 850$  to  $1900$ , in the low subcritical regime. In the absence of an understanding of the influence of Reynolds number, for the staggered configuration, the boundaries should be considered applicable only to the lower subcritical Reynolds number regime (for a single circular cylinder). However, some insight into how these boundaries may change with Reynolds number can be gained from a review of previous work on multiple cylinder configurations (Zdravkovich 1977, 1987, 1993; Nishimura 1986; Ohya *et al.* 1989). Essentially, significant Reynolds-number effects are mostly seen for the tandem configuration of two cylinders. The side-by-side configuration, on the other hand, is generally insensitive to Reynolds number, particularly in terms of the Strouhal number data and in a qualitative assessment of the flow patterns and their  $T/D$  boundaries (Sumner *et al.* 1999). Thus, the flow patterns and their boundaries identified for the staggered configuration, shown in figure 18, will be more sensitive to changes in Reynolds number when the tandem configuration is approached. Conversely, there will be less sensitivity to changes in Reynolds number when the staggered geometry is close to the side-by-side configuration.

Apart from changes to the boundaries, the number of flow patterns observed for a given Reynolds number may also change, depending on the flow regime. For example, Gu & Sun (1999) identified only three flow patterns for the staggered configuration in the high subcritical regime ( $Re = 2.2\text{--}3.3 \times 10^5$ ), namely 'Patterns  $I_B$ ,  $II_B$  and  $III_B$ ' (for the downstream cylinder). These patterns broadly correspond to the shear layer reattachment (SLR), induced separation (IS), and vortex pairing and enveloping (VPE, VPSE) patterns identified in the current study. The small number of flow patterns identified by Gu & Sun (1999) may be attributed to a limited range of  $P/D$  and  $\alpha$  used in their flow visualization experiments (see table 1), but it may also be a characteristic of the high subcritical regime, where local critical and supercritical flow conditions may be induced on one of the cylinders. Igarashi (1981, 1984), in his study of the tandem configuration, also noticed that the number of flow patterns observed was sensitive to Reynolds number. However, in the absence of other experimental evidence, at present it is not possible to predict the appearance of new flow patterns, or the disappearance of the flow patterns already identified here.

### 8.2. Bistable behaviour

The biased flow pattern observed for two side-by-side cylinders at intermediate  $T/D$  has been observed by some researchers to be bistable, i.e. the narrower and wider near-wake regions, and the direction of the gap flow, switch from one cylinder to the other (Sumner *et al.* 1999). When observed, the switching phenomenon occurs for periods much greater than the vortex shedding period, and it happens irregularly (Kim & Durbin 1988). Although a number of explanations for the bistable phenomenon have been proposed, Zdravkovich's (1987) explanation is based on the two-cylinder

staggered configuration. He proposed that bistability arises when the staggered configuration is at the 'critical' angle of incidence of  $\alpha = 90^\circ$ , between forward-stagger and rearward-stagger, at a geometry equivalent to the side-by-side configuration. The cylinder with the narrower near-wake region then acts as an 'upstream' cylinder, and the cylinder with the wider near-wake region acts as a 'downstream' cylinder. Based on the flow patterns identified in the present investigation, the forward- and rearward-stagger would involve the vortex pairing, splitting and enveloping (VPSE) and synchronized vortex shedding (SVS) flow patterns, respectively.

Within the staggered configuration, Zdravkovich (1987) contends that the bistable phenomenon extends to configurations with  $L/D = \pm 0.15$ , while Price & Païdoussis (1984) showed that for a small stagger of  $L/D = \pm 0.10$  bistability was no longer evident. In any case, the possibility of bistable behaviour in a staggered configuration means that, under certain conditions, a narrower near wake could form behind the downstream cylinder. Although bistable flow was not observed in any of the present experiments, an example was cited for the base-bleed (BB, §7.3) flow pattern of a narrower near-wake region behind the downstream cylinder (figure 8). However, this was observed only instantaneously, i.e. it was not a steady pattern, as would be the case for true bistable behaviour.

Bistable properties have also been found for mean lift coefficients by Zdravkovich & Pridden (1977), for a staggered configuration of  $L/D = 3.0$ ,  $T/D = 0.25$  ( $P/D = 3.01$ ,  $\alpha = 4.8^\circ$ ), at  $Re = 60\,000$ . Although the phenomenon was attributed to bistable gap flow, a more precise explanation may involve changes, back-and-forth, from the SLR flow pattern (§6.1) to the IS or VI flow patterns (§6.2 or §6.3, respectively), i.e. alternating between gap flow and no gap flow. This conclusion is supported by the mean static surface-pressure data of Zdravkovich & Pridden (1977), where one profile shows a (time-averaged) pressure minimum on the inner front face of the downstream cylinder, consistent with induced separation and vortex formation (IS) or vortex impingement (VI).

## 9. Interpretation of vortex shedding frequency measurements

The flow field of two staggered circular cylinders is often characterized by the occurrence of two vortex shedding frequencies. Previously, these two frequencies have been attributed to a higher frequency from the upstream cylinder, and a lower frequency from the downstream cylinder (Zdravkovich 1987). This study has shown, however, that the vortex shedding frequencies should more properly be associated with the individual shear layers rather than the cylinders. More specifically, vortex shedding from the inner shear layer of the downstream cylinder was often synchronized (at the same shedding frequency) with alternate Kármán vortex shedding from the two free shear layers of the upstream cylinder. Consequently, the two shear layers from the downstream cylinder shed vortices at different frequencies. This distinction was particularly evident in the VPE, VPSE and SVS flow patterns (figure 3g–i).

This study has also shown that vortex shedding from the upstream cylinder is nearly always present, particularly when there is flow through the gap between the cylinders. In prior studies, detection of only one Strouhal number, typically of lower value, implied the suppression of vortex shedding from the upstream cylinder (Zdravkovich 1987). In this study, the higher-frequency shedding from the upstream cylinder was absent only for the SBB1, SBB2, BB and SLR flow patterns (figure 3a–d).

These two important physical properties of the vortex shedding processes in the staggered configuration effectively confirm what Ishigai *et al.* (1972) noted: the



Strouhal number data for two staggered cylinders are strongly dependent on the measurement location. (Some of the results of Kiya *et al.* 1980, for example, would appear to show that vortex shedding from the upstream cylinder is absent.) To properly determine the number of fundamental frequencies associated with a given staggered geometry, measurements need to be made in the near-wake regions of each individual cylinder, in addition to the combined wake of the configuration. This approach also helps in the identification of their fluid dynamic origins. By determining the vortex shedding frequencies on a frame-by-frame basis from the flow visualization videos by counting and timing the individual vortices, this was to some extent realized in this study. A drawback of this approach (apart from the higher measurement uncertainty, see §3), is that lower-frequency events are more difficult to measure. This was especially apparent for the lower-frequency vortex shedding from the outer shear layer of the downstream cylinder, for two reasons. First, insufficient numbers of vortices were recorded on the video for accurate measurements. Second, vortex shedding from this shear layer had significant high-frequency modulation from the synchronized vortex formation of the other three shear layers, making counting difficult. Another drawback of this approach is that it fails to uncover any other high-frequency components that may be present in the flow.

Strouhal number data from this study, together with data from previously published work, are plotted against  $P/D$  and  $\alpha$  in figures 19 and 20, respectively. Since the experiments of Ishigai *et al.* (1972) and Moriya & Sakamoto (1985) were based on the  $L/D$  versus  $T/D$  notation, only some of their Strouhal number data could readily be converted into a  $P/D$  versus  $\alpha$  plot (for analysis at constant  $\alpha$  or  $P/D$ ) without using bilinear interpolation. Overall, the present results are consistent with those of other studies, although the lower Reynolds number range seems to yield greater values for the higher of the two Strouhal numbers detected. Differences in the experimental set-up, such as the cylinder aspect ratio, the solid blockage ratio, and the level of free-stream turbulence, will also contribute to the small differences in the Strouhal number data between the studies. This information is summarized in table 1. Kiya *et al.* (1980), however, failed to measure the very high frequencies of vortex formation which were found in the present study for the IS, VPE, and VPSE flow patterns (figure 3*e, g, h*). This is attributed to the location of their measuring probe, which was mostly situated in the combined wake of the two cylinders. Since it was rarely located in the interstitial region or behind the upstream cylinder, there is some scatter in  $St$  for  $\alpha = 0^\circ$  to  $30^\circ$  in figure 20(*a-d*).

### 9.1. Strouhal numbers at constant incidence

For staggered configurations of constant  $\alpha$ , an increase in  $P/D$  corresponds to a lessening of interference, and for each cylinder the vortex shedding becomes more like that for a single, isolated circular cylinder. Here, two different sets of Strouhal numbers are presented:  $\alpha = 25^\circ$  to  $35^\circ$  in figure 19(*a*) and  $\alpha = 55^\circ$  to  $65^\circ$  in figure 19(*b*). Each set of data represents a small range of staggered geometries of nearly constant incidence, of  $\alpha = 30^\circ$  and  $60^\circ$ , respectively. In each case, the variation of the Strouhal number with  $P/D$  is similar to that of two side-by-side cylinders (Sumner *et al.* 1997, 1999). At large pitch ratios, the Strouhal number approaches the value of  $St \sim 0.2$ , which corresponds to the Strouhal number for a single, isolated circular cylinder.

For the first set of data (figure 19*a*), corresponding to staggered configurations of smaller incidence,  $\alpha = 25^\circ$  to  $35^\circ$ , five flow patterns are included (SBB1, IS, VPE, VPSE, SVS; redefined in the figure caption) as  $P/D$  is increased. The SBB1

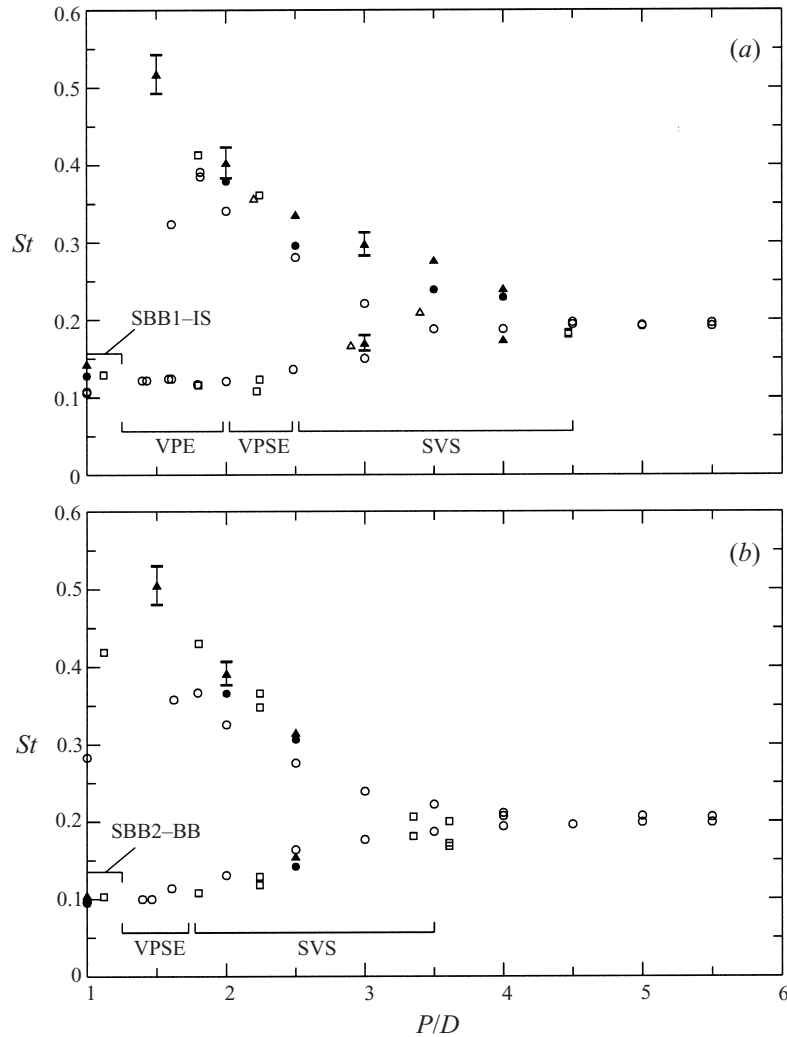


FIGURE 19. Strouhal number data for two staggered cylinders in steady upstream cross-flow: (a)  $\alpha = 25$  to  $35^\circ$ ; (b)  $\alpha = 55$  to  $65^\circ$ . ○, Kiya *et al.* (1980),  $Re = 17000$ ; □, Ishigai *et al.* (1972),  $Re = 1500$  to  $15000$ ; △, Moriya & Sakamoto (1985),  $Re = 65300$ ; ●, present study,  $Re = 1260$  to  $1350$ ; ▲, present study,  $Re = 820$  to  $930$ . Measurement uncertainty of 5% in the Strouhal number; representative error bars shown.

flow pattern corresponds to a single low-frequency vortex shedding, of  $St \sim 0.12$ , demonstrating single bluff-body behaviour with one vortex shedding process and one Kármán vortex street, since the cylinders are in contact (or very nearly in contact). As  $P/D$  is increased, and the flow moves away from the single bluff-body (SBB1) and induced separation (IS) flow patterns, a second high-frequency of vortex shedding is suddenly detected. (A second high-frequency may also be found for the IS flow pattern, see figure 20(b–e), but it is not shown in data for constant  $P/D$  in figure 19(a).) In the vortex pairing (VPE and VPSE) and synchronized vortex shedding (SVS) patterns that follow at higher pitch ratios, two frequencies of vortex shedding are found. The difference between these two frequencies becomes smaller as the cylinders are placed further apart and the wake interference is lessened. As this study

has shown, the higher Strouhal number is associated with vortex shedding both from the upstream cylinder and from the inner shear layer of the downstream cylinder. The lower Strouhal number is due to vortex shedding from the outer shear layer of the downstream cylinder. The smaller difference between the frequencies, with increasing  $P/D$ , is also seen in the Strouhal number data for two side-by-side cylinders (Sumner *et al.* 1997, 1999). It was shown in those studies that the difference correlates with the size difference of the two near-wake regions. As  $P/D$  is increased further, the two frequencies revert to a single frequency, at  $P/D \sim 4.5$ , where each cylinder now sheds vortices in a similar manner to a single, isolated circular cylinder, at  $St \sim 0.2$ . This result does not mean, however, that the interference of the second cylinder has disappeared, for there may still be anti-phase synchronization of the vortex streets (as noticed in the SVS flow pattern).

In the present study, two Strouhal numbers may be found at higher  $P/D$  than in other studies, similar to what was noticed for side-by-side cylinders (Sumner *et al.* 1997, 1999). This difference may be attributed to differences in Reynolds number, the influence of blockage and aspect ratio, or a combination of these effects. It is suspected that a similar difference occurs for  $\alpha = 60^\circ$ , but insufficient data were acquired at larger  $P/D$  to demonstrate this.

The second set of Strouhal data, in figure 19(b), corresponds to staggered configurations of greater incidence,  $\alpha = 55^\circ$  to  $65^\circ$ . Four flow patterns are observed in this range of incidence (SBB2, BB, VPSE, SVS) as  $P/D$  is increased. Similar characteristics to the smaller-incidence case, in figure 19(a), are seen, with a single low frequency for the SBB2 and BB flow patterns, and two frequencies for the VPSE and SVS patterns. (Some high frequencies found by other researchers, in the range of  $P/D$  corresponding to the SBB2 and BB flow patterns, are also shown in figure 19(b). Kiya *et al.* (1980) indicated that they may be associated with weaker and more broad-banded spectral peaks, but the higher frequencies were not detected in the present study.) The major difference between the two cases is the upper value of  $P/D$  at which a single value of  $St$  is first measured. Here, the larger-incidence staggered configuration (figure 19b) reverts to a single vortex shedding frequency, of  $St \sim 0.2$  at  $P/D \sim 3.5$  rather than at  $P/D \sim 4.5$ , as in the previous case (figure 19a). These two upper limits on the pitch ratio ( $P/D \sim 4.5$  for  $\alpha = 30^\circ$ , in figure 19(a), and  $P/D \sim 3.5$  for  $\alpha = 60^\circ$ , in figure 19(b)) may be linearly extended to  $P/D = 2.5$  for  $\alpha = 90^\circ$ , corresponding to the side-by-side configuration. The  $P/D = 2.5$  (or more properly,  $T/D = 2.5$ ) result agrees exactly with the upper limit of the biased flow pattern found in flow visualization experiments in the same water tunnel for two side-by-side cylinders (Sumner *et al.* 1997, 1999).

## 9.2. Strouhal numbers at constant pitch ratio

For staggered configurations of constant  $P/D$ , an increase in  $\alpha$  changes the geometry from the tandem configuration, at  $\alpha = 0^\circ$ , to the side-by-side configuration, at  $\alpha = 90^\circ$ . For smaller  $P/D$ , the increase in  $\alpha$  often means moving from a flow field with one Strouhal number, in nearly tandem configurations, to a flow field with two Strouhal numbers, in nearly side-by-side configurations, as shown in figure 20.

When the cylinders are in contact, at  $P/D = 1.0$  (figure 20a), single bluff-body behaviour with a single vortex shedding frequency is found for the entire range of incidence. At small angles of incidence,  $\alpha = 0^\circ$  to  $10^\circ$ , the single Strouhal number is higher than for a single, isolated circular cylinder, much as was observed for the tandem configuration at small  $L/D$  (Igarashi 1981, 1984; Ljungkrona 1992). Here, the higher frequency is caused by a shortening of the near-wake region, and corresponds

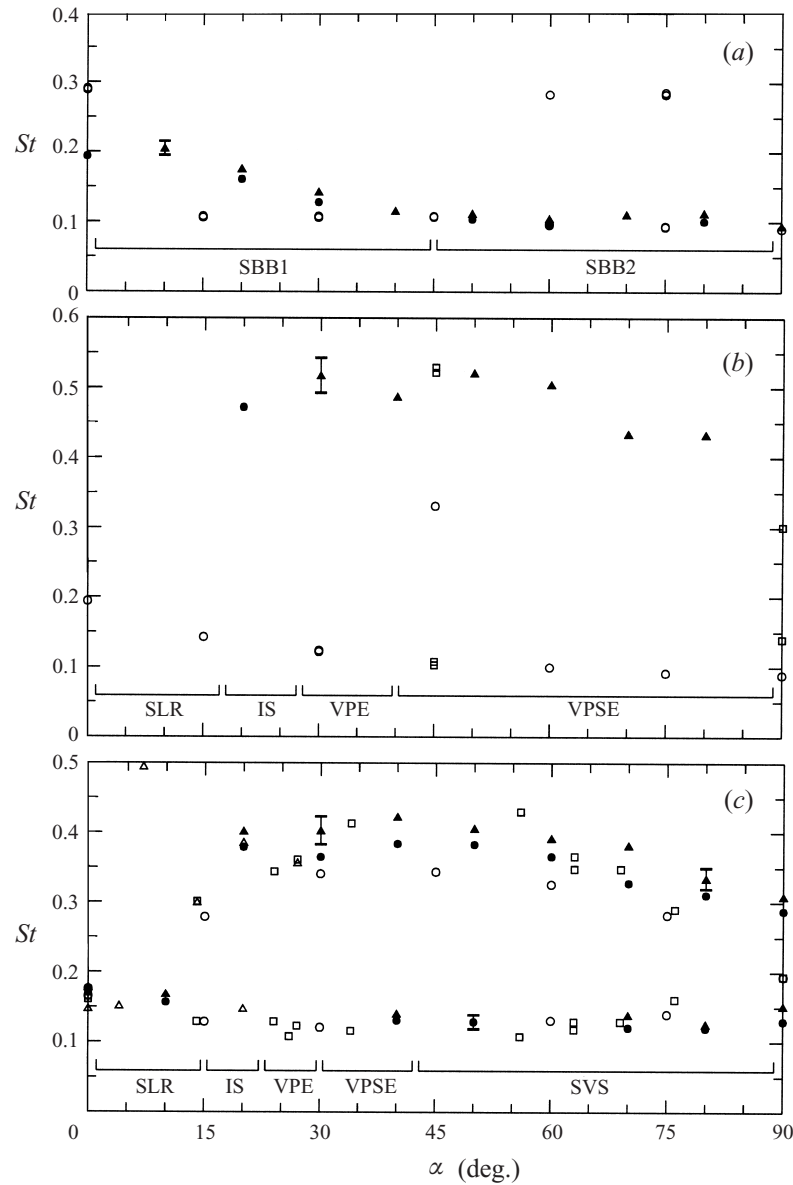


FIGURE 20. For caption see facing page.

to a portion of the type 1 single bluff-body (SBB1) flow pattern. From  $\alpha = 10^\circ$  to  $45^\circ$ , still within the SBB1 flow pattern, the Strouhal number steadily decreases to a value of  $St \sim 0.1$  (one-half the vortex shedding frequency for an isolated circular cylinder). The lowering of the Strouhal number occurs as the near-wake region lengthens and widens with increasing incidence. For  $\alpha > 45^\circ$ , the type 2 single bluff-body (SBB2) flow pattern is observed, and the Strouhal number remains relatively constant at  $St \sim 0.1$ , providing a good quantitative distinction between the SBB1 and SBB2 flow patterns. This Strouhal number is consistent with  $St = 0.1$  measured for two side-by-side cylinders in contact, at  $T/D = 1.0$  (Sumner *et al.* 1997, 1999). Although the data from Kiya *et al.* (1980) include some higher frequencies at  $\alpha = 60^\circ$  and  $75^\circ$

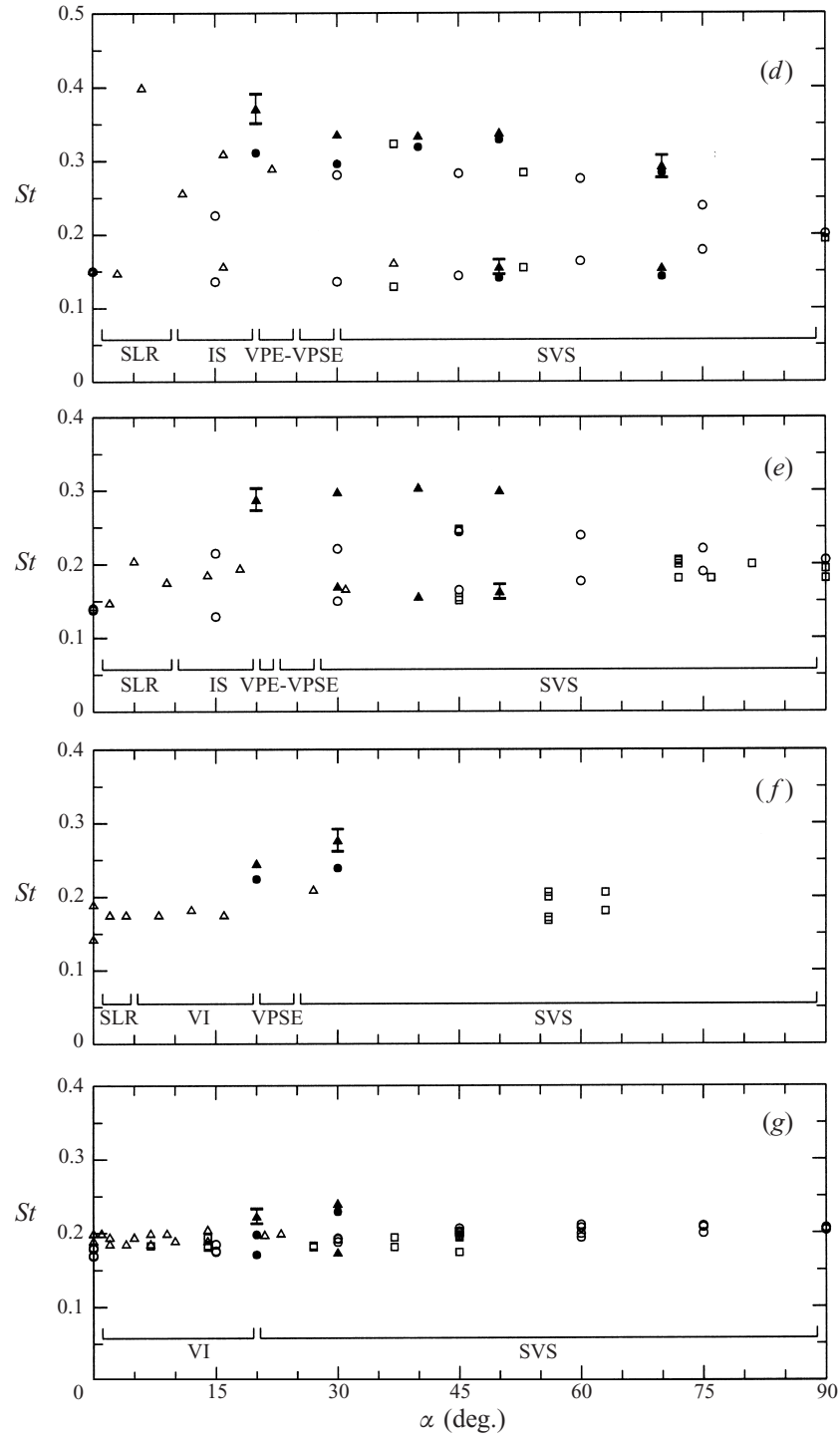


FIGURE 20. Strouhal number data for two staggered cylinders in steady upstream cross-flow: (a)  $P/D = 1.0$ ; (b)  $P/D = 1.4$  to  $1.6$ ; (c)  $P/D = 1.8$  to  $2.2$ ; (d)  $P/D = 2.5$  to  $2.7$ ; (e)  $P/D = 2.8$  to  $3.2$ ; (f)  $P/D = 3.4$  to  $3.6$ ; (g)  $P/D = 3.8$  to  $6.2$ . Symbols as in figure 19. Measurement uncertainty of 5% in the Strouhal number; representative error bars shown.

(shown in figure 20a), these were associated with weaker and more broad-banded spectral peaks, possibly unrelated to periodic vortex shedding.

For staggered configurations of  $P/D = 1.4$  to  $1.6$  (figure 20b), a single low vortex-shedding frequency is found for  $\alpha = 0^\circ$  to  $18^\circ$ , corresponding to the SLR flow pattern. Low-frequency shedding occurs from the cylinder group as a whole, by the interaction of the outer shear layers of the upstream and downstream cylinders. As in the case of the SBB1 flow pattern, shedding occurs at a frequency lower than that of a single cylinder. The low Strouhal number of  $St \sim 0.1$  persists at higher angles of incidence, up to and including the side-by-side configuration at  $\alpha = 90^\circ$ . A second Strouhal number four to five times higher appears at  $\alpha = 18^\circ$ , marking the transition from the shear layer reattachment (SLR) flow pattern to the induced separation (IS) flow pattern, as flow is deflected through the gap for the first time. Two vortex shedding frequencies are then found for the remaining angles of incidence, as the flow transitions to the vortex pairing (VPE and VPSE) patterns, although the difference between the high and low frequencies becomes smaller with increasing  $\alpha$ . The two shedding frequencies reflect the occurrence of vortex shedding from each of the cylinders. (In the present study, the low frequency could not be ‘measured’ reliably from the flow visualization video, because of high-frequency modulation from the pairing and enveloping process, and hence is absent in figure 20(b)).

Similar behaviour in the Strouhal number variation is also found at nominally constant pitch ratios of  $P/D = 2.0$  (actually,  $P/D = 1.8$  to  $2.2$ ) and  $2.5$  (actually,  $P/D = 2.5$  to  $2.7$ ), in figure 20(c,d), although there is an added transition to the synchronized vortex shedding (SVS) flow pattern. At these higher pitch ratios, however, the difference between the high and low Strouhal numbers becomes progressively smaller. Vortex shedding from the upstream cylinder, and the inner shear layer of the downstream cylinder (which occur at the same frequency), is now between three and four times greater than the lower-frequency shedding from the downstream cylinder (specifically, its outer shear layer). In both cases, a single vortex shedding frequency is found only for the shear layer reattachment (SLR) pattern. In figure 20(d), a single shedding frequency of  $St = 0.2$ , the same as that of a single cylinder, is also found at  $\alpha = 90^\circ$ , but this corresponds to the side-by-side configuration at the end of the biased flow pattern.

For the range of  $P/D = 2.8$  to  $3.2$  (figure 20e), the same flow patterns as in figure 20(c,d) are observed as  $\alpha$  is varied; however the lower of the two Strouhal numbers has increased towards the value for a single cylinder. In the range of incidence corresponding to the SVS flow pattern, two frequencies are no longer consistently observed; rather, from  $\alpha = 70^\circ$  to  $90^\circ$  only a single frequency is observed, meaning there is anti-phase synchronization of the two vortex streets, but both cylinders are now shedding at the same frequency.

The vortex impingement (VI) flow pattern first becomes evident at  $P/D = 3.5$ , for small  $\alpha$ , and is characterized by a single Strouhal number since both cylinders are believed to shed vortices at the same frequency. The single Strouhal number is shown in the data for  $P/D = 3.4$  to  $3.6$ , in figure 20(f), and  $P/D = 3.8$  to  $6.2$ , in figure 20(g). For these staggered configurations of high  $P/D$ , two vortex shedding frequencies are rarely detected, except within the VPSE flow pattern at  $P/D = 3.5$  (figure 20f), and for small ranges of incidence within the SVS flow pattern (figure 20f, g). Furthermore, the vortex shedding frequencies, whether low or high, now closely approximate vortex shedding from a single cylinder, near  $St = 0.2$ . This result does not indicate that no-interference conditions are established, however, since in most cases either the VI or SVS flow pattern exists.

## 10. Conclusions

In this study, a staggered configuration of two circular cylinders of equal diameter was examined under steady upstream cross-flow conditions in the low subcritical Reynolds number regime ( $Re = 850$  to  $1900$ ). Prior studies of the staggered configuration have mostly been restricted to the higher subcritical regime ( $Re = 10^4$  to  $10^5$ ). By following a flow-pattern approach, the complexity of the fluid behaviour was revealed as  $P/D$  and  $\alpha$  were each separately varied over wide ranges (from  $P/D = 1.0$  to  $5.0$ , and from  $\alpha = 0^\circ$  to  $90^\circ$ ). In this portion of the low subcritical regime, nine different flow patterns were identified. The pitch ratio and incidence angle boundaries for the flow patterns were also proposed. Important features of the flow include shear layer reattachment, induced separation, vortex pairing and synchronization, and vortex impingement. In some cases, very small changes in the incidence, or direction of the oncoming flow, result in a very different flow pattern. The complexity of the flow may be attributed, in part, to two findings.

First, for the majority of flow patterns, there exists some form of vortex shedding from the upstream cylinder, which is intrinsically linked with the flow through the gap between the cylinders. This vortex shedding from the upstream cylinder can occur even for staggered configurations of very small incidence and pitch ratio. Its frequency is typically higher than that measured in the near-wake region of the downstream cylinder. Furthermore, the frequency may be missed if the only information available to the observer is a velocity-time signal at a single point in the combined wake of the two cylinders. This result means that the potential for vortex-induced vibrations, at multiple frequencies, may still exist even for cylinders in close proximity. This observation contradicts a contention by Zdravkovich (1985) that strong gap flow can occur in the absence of vortex shedding from the upstream cylinder.

Second, by using video rather than still photography, the origins of the two vortex shedding frequencies, one low and the other high, that are commonly detected were clarified. In particular, the two frequencies are more properly associated with the individual free shear layers, rather than with the individual cylinders. In this manner, the two shear layers from the rearmost cylinder, in many cases, do not shed vortices at the same, lower frequency. Instead, the two shear layers act independently, with only the outer shear layer shedding Kármán vortices of low frequency. Vortex shedding from the inner shear layer of the downstream cylinder is instead synchronized with higher-frequency Kármán vortex shedding from the upstream cylinder. This distinction may promote a rethinking of how Strouhal number data for the staggered configuration ought to be interpreted. From a design point-of-view, when considering the causes of flow-induced vibrations, this may be invaluable.

The flow pattern boundaries now make it possible to predict more accurately the nature of the flow for a given geometry of two cylinders. More specifically, it may now be possible to identify the fluid dynamic origins for various phenomena noted by other researchers in their measurements of lift and drag force coefficients. Furthermore, it may now be possible to identify which flow patterns present situations in which the cylinders are more susceptible to flow-induced vibrations. Prior studies which report extensive force measurements (Zdravkovich & Pridden 1977; Moriya & Sakamoto 1985) have been conducted at much higher Reynolds numbers ( $Re = 60\,000$  to  $65\,300$ ) than in the present study, however. It is not yet known precisely how these flow-pattern boundaries will change with the Reynolds number, or indeed if the number of flow patterns observed will change. Indeed, a study of the influence of the Reynolds number remains to be undertaken for the staggered cylinder configuration, and this is

a prime subject for further research. Certainly, the statement by Gu & Sun (1999), that it is reasonable to presume that similar flow patterns should be observed throughout the subcritical regime, remains to be substantiated. A cursory study of the flow patterns from the present study indicates that the inner maximum lift curve, identified by Zdravkovich & Pridden (1977), is probably caused by the induced separation (IS) flow pattern identified here. Furthermore, the disappearance of the inner maximum lift curve with a reduction in  $T/D$ , also noticed by Zdravkovich & Pridden (1977), would be consistent with a changeover to the shear layer reattachment (SLR) flow pattern. Gu & Sun (1999) arrived at much the same conclusions, when considering the pressure distributions on the downstream cylinder responsible for their 'Patterns I<sub>B</sub> and II<sub>B</sub>'. However, for the time being these conclusions are only conjectural, since there is an absence of force measurements within the lower subcritical regime.

The authors would like to acknowledge the financial support of the Natural Sciences and Engineering Research Council of Canada (NSERC) and Les Fonds FCAR du Québec. The assistance of S. S. T. Wong, who conducted the flow visualization experiments, is also gratefully acknowledged.

#### REFERENCES

- CANTWELL, B. & COLES, D. 1983 An experimental study of entrainment and transport in the turbulent near wake of a circular cylinder. *J. Fluid Mech.* **136**, 321–374.
- GU, Z. F. & SUN, T. F. 1999 On interference between two circular cylinders in staggered arrangement at high subcritical Reynolds numbers. *J. Wind Engng Indust. Aerodyn.* **80**, 287–309.
- GURSUL, I. & ROCKWELL, D. 1990 Vortex street impinging upon an elliptical leading edge. *J. Fluid Mech.* **211**, 211–242.
- IGARASHI, T. 1981 Characteristics of the flow around two circular cylinders arranged in tandem (1st report). *Bull. JSME* **24**, 323–331.
- IGARASHI, T. 1984 Characteristics of the flow around two circular cylinders arranged in tandem (2nd report, unique flow phenomenon at small spacing). *Bull. JSME* **27**, 2380–2387.
- ISHIGAI, S., NISHIKAWA, E., NISHIMURA, K. & CHO, K. 1972 Experimental study of structure of gas flow in tube banks with tube axes normal to flow (Part I, Kármán vortex flow from two tubes at various spacings). *Bull. JSME* **15**, 949–956.
- ISHIGAI, S., NISHIKAWA, E. & YAGI, E. 1973 Structure of gas flow and vibration in tube banks with tube axes normal to flow. In *Proc. Int. Symp. on Marine Engineering, Tokyo, Japan*, pp. 1-5-2 to 1-5-33.
- KIM, H. J. & DURBIN, P. A. 1988 Investigation of the flow between a pair of circular cylinders in the flopping regime. *J. Fluid Mech.* **196**, 431–448.
- KIYA, M., ARIE, M., TAMURA, H. & MORI, H. 1980 Vortex shedding from two circular cylinders in staggered arrangement. *Trans. ASME: J. Fluids Engng* **102**, 166–173.
- LAM, K. & CHEUNG, W. C. 1988 Phenomena of vortex shedding and flow interference of three cylinders in different equilateral arrangements. *J. Fluid Mech.* **196**, 1–26.
- LAM, K. & LO, S. C. 1992 A visualization study of cross-flow around four cylinders in a square configuration. *J. Fluids Struct.* **6**, 109–131.
- LJUNGKRONA, L. 1992 Characteristics of mean and fluctuating surface pressure distributions on tubes in tandem arrangement and in-line tube bundles. PhD thesis, Department of Thermodynamics and Fluid Dynamics, Chalmers University of Technology, Göteborg, Sweden.
- MORIYA, M. & SAKAMOTO, H. 1985 Fluctuating fluid forces acting on a downstream circular cylinder in the staggered arrangement. *Trans. JSME* **51**, 2098–2104 (in Japanese).
- NISHIMURA, T. 1986 Flow across tube banks. In *Encyclopedia of Fluid Mechanics – Flow Phenomena and Measurement*, Vol. 1 (ed. N. P. Cheremisinoff), pp. 763–785. Gulf.
- OENGGÖREN, A. & ZIADA, S. 1995 Vortex shedding, acoustic resonance and turbulent buffeting in normal triangle tube arrays. In *Flow-Induced Vibration* (ed. P. W. Bearman), *Proc. Sixth Intl Conf. on Flow-Induced Vibration*, London, UK, pp. 295–313, A. A. Balkema.



- OHYA, Y. O., OKAJIMA, A., & HAYASHI, M. 1989 Wake interference and vortex shedding. In *Encyclopedia of Fluid Mechanics – Aerodynamics and Compressible Flow*, Vol. 8 (ed. N. P. Chermisinoff), pp. 322–389. Gulf.
- PRICE, S. J. 1976 The origin and nature of the lift force on the leeward of two bluff bodies. *Aero. Q.* **27**, 154–168.
- PRICE, S. J. & PAÏDOUSSIS, M. P. 1984 The aerodynamic forces acting on groups of two and three circular cylinders when subject to a cross-flow. *J. Wind Engng Indust. Aerodyn.* **17**, 329–347.
- ROCKWELL, D. 1998 Vortex-body interactions. *Ann. Rev. Fluid Mech.* **30**, 199–229.
- SCHMIDT, D. W. & TILMANN, P. M. 1972 Über die Zirkulationsentwicklung in Nachläufen von Rundstäben. *Acustica* **27**, 14–22 (in German).
- SUMNER, D. 1999 Circular cylinders in cross-flow. PhD thesis, Department of Mechanical Engineering, McGill University, Montréal, Canada.
- SUMNER, D., WONG, S. S. T., PRICE, S. J. & PAÏDOUSSIS, M. P. 1997 Two and three side-by-side circular cylinders in steady cross-flow. In *Proc. 16th Canadian Congress of Applied Mechanics, Québec City, Canada* (ed. L. Cloutier & D. Rancourt), pp. 273–274.
- SUMNER, D., WONG, S. S. T., PRICE, S. J. & PAÏDOUSSIS, M. P. 1999 Fluid behaviour of side-by-side circular cylinders in steady cross-flow. *J. Fluids Struct.* **13**, 309–338.
- SUN, T. F., GU, Z. F., HE, D. X. & ZHANG, L. L. 1992 Fluctuating pressure on two circular cylinders at high Reynolds numbers. *J. Wind Engng Indust. Aerodyn.* **41–44**, 577–588.
- SUZUKI, N., SATO, H., IUCHI, M. & YAMAMOTO, S. 1971 Aerodynamic forces acting on circular cylinders arranged in a longitudinal row. In *Wind Effects on Buildings and Structures, Intl Wind Conf., Tokyo*, Part II, pp. 20-1 to 20-10.
- SZEPESY, S. 1993 On the control of circular cylinder flow by end plates. *Eur. J. Mech. B/Fluids* **12**, 217–244.
- TANAKA, S. & MURATA, S. 1986 An investigation of the wake structure of a circular cylinder using a computer aided flow visualization (1st report, generation and dissipation at the vorticity). *Bull. JSME* **29**, 1446–1454.
- TING, D. S.-K., WANG, D. J., PRICE, S. J. & PAÏDOUSSIS, M. P. 1998 An experimental study on the fluidelastic forces for two staggered circular cylinders in cross-flow. *J. Fluids Struct.* **12**, 259–294.
- WILLERT, C. & GHARIB, M. 1991 Digital particle image velocimetry. *Exps Fluids* **10**, 181–193.
- WILLIAMSON, C. H. K. 1985 Evolution of a single wake behind a pair of bluff bodies. *J. Fluid Mech.* **159**, 1–18.
- ZDRAVKOVICH, M. M. 1977 Review of flow interference between two circular cylinders in various arrangements. *Trans. ASME. J. Fluids Engng* **99**, 618–633.
- ZDRAVKOVICH, M. M. 1985 Flow induced oscillations of two interfering circular cylinders. *J. Sound Vib.* **101**, 511–521.
- ZDRAVKOVICH, M. M. 1987 The effects of interference between circular cylinders in cross flow. *J. Fluids Struct.* **1**, 239–261.
- ZDRAVKOVICH, M. M. 1993 Interstitial flow field and fluid forces. In *Technology for the 90s: A Decade of Progress* (ed. M. K. Au-Yang). ASME.
- ZDRAVKOVICH, M. M. & PRIDDEN, D. L. 1977 Interference between two circular cylinders; series of unexpected discontinuities. *J. Indust. Aerodyn.* **2**, 255–270.